Ocean and Coastal Area Information Retrieval Using SAR Polarimetry

Andrea Buono, Emanuele Ferrentino, Yu Li, and Carina Regina de Macedo

List of Abbreviations

ALOS	Advanced Land Observing Satellite
AOI	Angle of Incidence
ASAR	Advanced SAR
ASI	Italian Space Agency
BSA	Back Scattering Alignment
CFAR	Constant False Alarm Rate
CNN	Convolutional Neural Network
CONAE	National Commission of Space Activities
CP	Compact Polarimetric
CPD	Co-polarized Phase Difference
CSA	Canadian Space Agency
CSG	CSK Second Generation

A. Buono (✉)
University of Naples Parthenope, Naples, Italy
e-mail: andrea.buono@uniparthenope.it

E. Ferrentino
National Institute of Geophysics and Volcanology, Rome, Italy
e-mail: emanuele.ferrentino@ingv.it

Y. Li
Beijing University of Technology, Beijing, China
e-mail: yuli@bjut.edu.cn

C. R. de Macedo
University of the Littoral Côte d'Opale, UMR 8187 - LOG - Laboratoire d'Océanologie et de Géosciences, Wimereux, France

CNRS, UMR 8187, Lille, France

University of Lille, Lille, France
e-mail: carina.macedo@fc.up.pt

M. Rysz et al. (eds.), *Synthetic Aperture Radar (SAR) Data Applications*, Springer Optimization and Its Applications 199, https://doi.org/10.1007/978-3-031-21225-3_10

CSK	Cosmo Sky-Med
CTLR	Circular Transmit Linear Receive
CVCNN	Complex-Valued CNN
dB	Decibel
DBN	Deep Belief Network
DLR	German Aerospace Center
DOP	Degree of Polarization
DP	Dual Polarimetric
ENVISAT	ENVIronmental SATellite
ESA	European Space Agency
FP	Full Polarimetric
HH	Horizontal transmit horizontal receive
HV	Horizontal transmit vertical receive
ISRO	Indian Space Research Organization
JAXA	Japanese Aerospace eXploration Agency
NESZ	Noise Equivalent Sigma Zero
NPH	Normalized Pedestal Height
NRCS	Normalized Radar Cross Section
PALSAR	Phased Array L-band SAR
PD	Polarization Difference
PolSAR	Polarimetric SAR
PR	Polarization Ratio
PSD	Power Spectral Density
PTSM	Polarimetric TSM
RCM	Radarsat Constellation Mission
RVCNN	Real-Valued CNN
SAE	Sparse Auto-Encoder
SAOCOM	Microwave Observing Argentinian Satellite
SAR	Synthetic Aperture Radar
SGD	Stochastic Gradient Descent
SIR	Spaceborne Imaging Radar
SNR	Signal-to-Noise Ratio
SPM	Small Perturbation Method
SVM	Support Vector Machine
TSM	Two-Scale Model
UAVSAR	Unmanned Aerial Vehicle SAR
VV	Vertical transmit vertical receive

1 Radar Polarimetry

This section presents a general overview of the theoretical background needed to model the sea surface polarimetric observables. We focus on the general formulation of the polarimetric scattering process that describes the electromagnetic interaction between the wave transmitted by a microwave sensor and a target to be observed on the Earth's surface.

In this section, we first introduce the mathematical formalism used to describe polarimetric observables in Sect. 1.1. Then, in Sect. 1.2, an overview of the operational and planned polSAR systems and the main characteristics of the polarimetric imaging modes is provided. As a reference, information about multi-polarization

models to describe sea surface scattering is given in Sect. 1.3. Finally, in Sect. 1.4, meaningful experimental showcases are presented to demonstrate some of the most representative polarimetric properties of sea surface scattering.

1.1 Polarimetric Scattering Descriptors

In this subsection, a general overview of the polarimetric scattering descriptors of the electromagnetic interaction between the transmitted wave and the observed surface is presented.

Considering a monostatic radar sensor, a microwave pulse transmitted by a radiation source interacts with the observed surface, and it is scattered back to be received by the original transmitting antenna. The received electromagnetic pulse brings information about the scene that can be accessed taking into account the transmitted and received waves. According to the Jones formalism, in the far zone of the scatter, the transformation of the incident wave into the scattered one is given in Eq. (1), where the transformation is ruled by the scattering matrix $\boldsymbol{S}$ [34]:

$$\mathbf{E}^s = \frac{e^{-jkr}}{r}\boldsymbol{S}\mathbf{E}^i, \tag{1}$$

where the ratio e^{-jkr}/r is the spherical wave factor with j being the imaginary unit, k the electromagnetic wave number, and r the distance between the SAR antenna and the center of the scene. $\mathbf{E}^s$ and $\mathbf{E}^i$ are the complex Jones vectors describing, respectively, the scattered and incident waves.

Considering the monostatic backscattering case, i.e., the transmitting and receiving antennas are in the same location, and under the backscatter alignment convention (BSA), the scattering matrix $\boldsymbol{S}$ is a 2×2 complex-valued matrix also known as Sinclair matrix and, adopting the linear horizontal (h)–vertical (v) polarization basis and considering the propagation through a reciprocal medium, can be given by

$$\boldsymbol{S} = \begin{pmatrix} S_{hh} & S_{hv} \\ S_{hv} & S_{vv} \end{pmatrix} = \begin{pmatrix} |S_{hh}|\, e^{j\varphi_{hh}} & |S_{hv}|\, e^{j\varphi_{hv}} \\ |S_{hv}|\, e^{j\varphi_{hv}} & |S_{vv}|\, e^{j\varphi_{vv}} \end{pmatrix} = e^{j\varphi_{hh}} \begin{pmatrix} |S_{hh}| & |S_{hv}|\, e^{j\varphi_x} \\ |S_{hv}|\, e^{j\varphi_x} & |S_{vv}|\, e^{j\varphi_c} \end{pmatrix}, \tag{2}$$

where S_{pq}, with $p, q \in \{h, v\}$, is the complex scattering amplitude, while $S_{vh} = S_{hv}$ results from the reciprocity assumption. The diagonal and off-diagonal terms of the scattering matrix $\boldsymbol{S}$ call for, respectively, the same (termed co-polar) and orthogonal (cross-polar) polarization for both incident and scattered waves. $|S_{pq}|$ are the modulus of the scattering amplitude, and φ_c and φ_x are the relative phase between, respectively, the co-polarized and the cross-polarized channels:

$$\varphi_c = \varphi_{hh} - \varphi_{vv} \quad , \quad \varphi_x = \varphi_{hv} - \varphi_{hh}. \tag{3}$$

The phase differences between co-polarized and cross-polarized channels are often indicated as CPD and XPD, respectively. The Jones formalism shown in Eq. (1) represents a first-order coherent scattering model (i.e., a completely polarized and deterministic scattering) and does not allow describing the phenomena of depolarization that may arise from the scattering of random and distributed scenes. The second-order descriptors are used to deal with the polarimetric scattering from the distributed and depolarizing scenes based on both an incoherent and coherent approaches. The latter is based on the coherency $\boldsymbol{T}$ and covariance $\boldsymbol{C}$ matrix, while the former on the Stokes formalism where the 4×4 Muller matrix $\boldsymbol{M}$ connects the partially polarized scattered wave ($\mathbf{g}^s$) to the fully polarized incident wave ($\mathbf{g}^i$) [34]:

$$\mathbf{g}^s = (kr)^{-2} \langle \boldsymbol{M} \rangle \mathbf{g}^i, \tag{4}$$

where $\langle \cdot \rangle$ denotes ensemble average, the matrix $\boldsymbol{M}$ is real and never symmetric, its elements are ensemble averages of combinations of scattering amplitudes, and more details can be found in [33, 34]. The Stokes vector $\mathbf{g}$ represents the polarization properties of an electromagnetic plane wave based on non-coherent power measurements. The Stokes vector, different from the Jones formalism, can describe partially polarized waves. In Eq. (4), since the incidence wave is deterministic, no ensemble average is made in $\mathbf{g}^i$. According to the Stokes formalism, the degree of polarization (DOP) of a partially polarized target can be evaluated:

$$\mathrm{DOP} = \frac{\sqrt{{g_1}^2 + {g_2}^2 + {g_3}^2}}{{g_0}^2}. \tag{5}$$

The DOP is a basis-invariant parameter ranging between 0 and 1 that measures the amount of polarized scattering/component of the target/electromagnetic wave.

One of the most powerful tools that characterize polSAR is the polarization synthesis, i.e., the synthesis of the power given the polarization properties of any couple of transmitting/receiving antenna once a complete polarimetric measure has been performed in an orthogonal basis. The normalized radar cross section (NRCS) can be evaluated based on the Kennaugh matrix, $\boldsymbol{K}$, for any possible combination of transmitting/receiving antenna polarizations, assuming that the antennas match in both load and polarization:

$$\sigma^0 = \frac{4\pi}{2k^2} \left\langle \mathbf{g}^r \right\rangle^T \langle \boldsymbol{K} \rangle \mathbf{g}^t, \tag{6}$$

where the superscript T is the transpose operator, and $\mathbf{g}^t$ and $\mathbf{g}^r$ are, respectively, the transmitted and received polarizations described using the Stokes formalism. Considering the BSA convention, $\boldsymbol{K}$ is given by Guissard [34]

$$\boldsymbol{K} = \mathrm{diag}(1, 1, 1, -1)\boldsymbol{M}. \tag{7}$$

Once polarization synthesis is performed, by varying the transmitting/receiving polarization couple, the NRCS can be plotted versus both the tilting Φ and the ellipticity χ angles, i.e., for any polarization. Hence, the co-polarized (transmitting and receiving polarizations call for the same Stokes vector) and cross-polarized (transmitting and receiving polarizations call for the orthogonal Stokes vectors) signatures of the target are obtained. Once the former is normalized with respect to the total backscattered power, namely the SPAN, the normalized pedestal height (NPH) can be derived, which is the lowest NRCS in the normalized co-polarized signature, while varying the tilting and ellipticity angles (i.e., the polarization). The NPH describes the amount of unpolarized energy with respect to the total received power.

The Mueller matrix is in a one-to-one mapping with the coherency matrix $\boldsymbol{T}$ [16, 48]. The latter completely describes the polarimetric scattering properties of a generic distributed and depolarizing scene with the advantage of, unlike the Mueller matrix, being Hermitian and semi-definite positive matrices. The latter properties allow the decomposition of the $\boldsymbol{T}$ and $\boldsymbol{C}$ matrices in elementary scattering mechanisms providing a physical interpretation of the scene scattering processes. The coherency/covariance matrices are both ensemble averages of combinations of scattering amplitudes. Considering the backscattering case and assuming reciprocity, the coherency matrix $\boldsymbol{T}$ and the covariance matrix $\boldsymbol{C}$ can be expressed, respectively, as [16]

$$\begin{aligned}\boldsymbol{T} &= \left\langle \mathbf{k}\mathbf{k}^{\dagger} \right\rangle \\ &= \frac{1}{2}\begin{pmatrix} \langle |S_{hh}+S_{vv}|^2 \rangle & \langle (S_{hh}+S_{vv})(S_{hh}-S_{vv})^* \rangle & 2\langle (S_{hh}+S_{vv})S_{hv}^* \rangle \\ \langle (S_{hh}-S_{vv})(S_{hh}+S_{vv})^* \rangle & \langle |S_{hh}-S_{vv}|^2 \rangle & 2\langle (S_{hh}-S_{vv})S_{hv}^* \rangle \\ 2\langle S_{hv}(S_{hh}+S_{vv})^* \rangle & 2\langle S_{hv}(S_{hh}-S_{vv})^* \rangle & 4\langle |S_{hv}|^2 \rangle \end{pmatrix}\end{aligned} \tag{8}$$

and

$$\boldsymbol{C} = \left\langle \mathbf{k}\mathbf{k}^{\dagger} \right\rangle = \begin{pmatrix} \langle |S_{hh}|^2 \rangle & \sqrt{2}\langle S_{hh}S_{hv}^* \rangle & \langle S_{hh}S_{vv}^* \rangle \\ \sqrt{2}\langle S_{hv}S_{hh}^* \rangle & 2\langle |S_{hv}|^2 \rangle & \sqrt{2}\langle S_{hv}S_{vv}^* \rangle \\ \langle S_{vv}S_{hh}^* \rangle & \sqrt{2}\langle S_{vv}S_{hv}^* \rangle & \langle |S_{vv}|^2 \rangle \end{pmatrix}, \tag{9}$$

where $\mathbf{k}$ is the target scattering vector projected into the Pauli (lexicographic) basis [16]. The $\boldsymbol{T}$ matrix can be uniquely diagonalized as follows:

$$\boldsymbol{T} = \boldsymbol{U}\boldsymbol{D}\boldsymbol{U}^{-1} = \sum_{i=1}^{3} \lambda_i \mathbf{u}_i \cdot \mathbf{u}_i^{\dagger} = \boldsymbol{T}_1 + \boldsymbol{T}_2 + \boldsymbol{T}_3. \tag{10}$$

Equation (10) describes the decomposition of the $\boldsymbol{T}$ matrix into the sum of three elementary scattering mechanisms (i.e., surface scattering from a plane flat structure, double-bounce scattering from a dihedral structure, and volume scattering from a randomly oriented cloud of dipoles) described by the eigenvectors $\mathbf{u}_i$ in

which the power contribution for each mechanism is given by the eigenvalues λ_i [16, 48]. Since $\boldsymbol{T}$ matrix satisfies Hermitian symmetry and is semi-definite positive, it is characterized by real non-negative eigenvalues that satisfy the following relationship:

$$\lambda_1 \geq \lambda_2 \geq \lambda_3 \geq 0. \tag{11}$$

$\boldsymbol{T}$ and $\boldsymbol{C}$ matrices share the same eigenvalues, and their eigenvectors are linked to each other by a con-similarity transformation [16, 48]:

$$\boldsymbol{C} = \boldsymbol{F}^{-1}\boldsymbol{T}\boldsymbol{F} \quad , \quad \boldsymbol{F} = \frac{1}{\sqrt{2}}\begin{pmatrix} 1 & 0 & 1 \\ 1 & 0 & -1 \\ 0 & \sqrt{2} & 0 \end{pmatrix}. \tag{12}$$

The eigen-decomposition of the coherency matrix results in meaningful basis-invariant synthetic parameters that are strictly related to the scattering properties of the observed target. The polarimetric entropy, H, is given by

$$H = -\sum_{i=1}^{3} p_i \log_3 (p_i) \quad , \quad p_i = \frac{\lambda_i}{\sum_{j=1}^{3} \lambda_j}, \tag{13}$$

while the mean scattering angle $\bar{\alpha}$ is defined by

$$\bar{\alpha} = \sum_{i=1}^{3} \frac{\lambda_i}{\sum_{j=1}^{3} \lambda_j} \cos^{-1}(|\mathbf{u}_i(1)|). \tag{14}$$

The entropy H is a basis-invariant measure, bounded between 0 and 1, of the randomness of polarimetric scattering mechanisms that characterize the observed target. $H = 0$ means deterministic scattering, while $H = 1$ means completely unpolarized scattering. The mean scattering angle $\bar{\alpha}$, ranging between 0 and 90°, represents the average scattering mechanism of the target. $\bar{\alpha} = 0°$, 45°, and 90° stand for surface, volume, and double-bounce scattering, respectively.

The eigenvalues of the coherency/covariance matrices can also be used to express the NPH:

$$\text{NPH} = \frac{\lambda_3}{\lambda_1}. \tag{15}$$

1.2 PolSAR Imaging Modes

In this subsection, a brief overview of polarimetric SAR missions is presented.

In the last decades, SAR satellites were launched acquiring information from the Earth surface at different microwave wavelengths and exploiting as well different polarimetric and imaging modes. Since the polarimetric SAR provides reliable, detailed, and valuable information on the physical properties and processes that rule the observed scene, spaceborne polarimetric missions were launched recently or are planned to be launched in the next years (e.g., the BIOMASS mission that consists of a P-band SAR that will focus on the global distribution of forest biomass). An overview of the main polSAR spaceborne missions is provided in Table 1.

According to the polarimetric information content, the SAR can be classified as full polarimetric (FP), dual polarimetric (DP), and compact polarimetric (CP). The FP SAR transmits and receives radiation on an orthogonal linear polarization basis, providing the complete scattering matrix information on the observed scene. Operational SAR missions are continuously acquiring information at different frequencies, e.g., the C-band CSA (Canadian Space Agency), Radarsat-2, the L-band JAXA (Japanese Aerospace Exploration Agency), Alos (Advanced Land Observing Satellite), PalSAR-2 (Phased Array Type L-band SAR), and the X-band ASI (Italian Space Agency), CSG (Constellation of Small Satellites for the Mediterranean Basin Observation). The planned biomass mission will be equipped with a FP SAR. An important limitation related to the FP SARs is related to its limited area coverage (a swath smaller than 70 km) that impacts directly on its use for operational monitoring services.

When compared to the FP SAR systems, the DP ones provide less polarimetric information, i.e., they transmit a single linear polarization and receive usually both amplitude and phase (coherently) in the corresponding orthogonal basis, providing a single row/column of the scattering matrix, see Eq. (2). However, as advantage, the DP SAR missions offer doubled area coverage when compared with the FP systems. The operational DP SARs we can mention are the X-band ASI CSK, calling for an incoherent DP imaging mode (i.e., alternating bursts are transmitted/received, so no phase link is measured between the two polarimetric channels), the X-band DLR (German Aerospace Center), TerraSAR-X, and C-band ESA (European Space Agency), Sentinel-1.

A single circular or slant linear polarization is transmitted by the CP SAR architectures and is then received according to the linear orthogonal basis. The CP SAR system only measures the wave coherency matrix associated to the received electromagnetic wave, limiting the amount of scattering information that can be extracted when compared to FP missions. Even though the information received by the CP system is biased and/or dependent on the considered CP mode, CP SAR data have been successfully exploited for coastal areas observation [77]. CP SAR missions are a trade-off solution between the area coverage and the amount of polarimetric information. CP SAR satellites have been launched recently, for example, the L-band CONAE (National Space Activities Commission) SAOCOM

Table 1 Operational and planned spaceborne polarimetric missions. The information listed refers to the finest spatial resolution polarimetric mode

Mission/SAR	Agency	Launch	Mode	Frequency band	NESZ (dB)	Spatial resolution (slant rg. x az.) (m)	Area coverage (rg. x az.) (km)
Radarsat-2	CSA	2007	DP, FP	C	-36.5 ± 3	5.2×7.6	25×25
CSK	ASI	2007	DP	X	≤ -22	15×15	30×30
TerraSAR-X	DLR	2007	DP, FP	X	-19 — -26	1.2×2.2	10×5
RISAT-1	ISRO	2012	DP, CP, FP	C	≤ -19	4×9	25×25
Alos PalSAR-2	JAXA	2014	DP, CP, FP	L	-28	10×10	30×30
Sentinel-1	ESA	2014	DP	C	≤ -22	5×5	80×80
SAOCOM	CONAE	2018	DP, CP, FP	L	≤ -25	10×10	20×20
RCM	CSA	2019	DP, CP, FP	C	≤ -24	9×9	20×20
CSG	ASI	2019	DP, FP	X	≤ -19	3×3	40×15
BIOMASS	ESA	2023	DP, CP, FP	0.4, P	≤ -24	$\leq 50 \times 50$	2×60

(Argentine Microwaves Observation Satellite), and the C-band CSA RCM (Radarsat Constellation Mission). Another operational mission that has an CP SAR is the C-band ISRO (Indian Space Research Organization), RISAT-1 (Radar Imaging SATellite).

To acquire data from the Earth's surface, different operational modes can be used by the SAR systems. The most fundamental and simplest mode is the stripmap where the radar antenna is fixed to one swath and draws a strip on the ground during the time in which the platform moves. The illuminated area in the Earth's surface is limited in the range size and theoretically unlimited in the along-track (azimuth) direction [22]. Taking the TerraSAR-X system as example, when working on stripmap mode, its standard scene size is 30 × 50 km (range × azimuth) and its spatial resolution is 1.2 × 3.3 m (slant range × azimuth) for single polarization and, respectively, 15 × 50 km and 1.2 × 6.6 m for dual polarization.

In case a wider swath is needed, the antenna can be operated on scanSAR mode where, to illuminate different range subswaths, the antenna beam elevation is periodically switched. In this case, the azimuth resolution is degraded compared to stripmap mode [22]. The standard scene size for the TerraSAR-X system operating on scanSAR mode is 100 × 150 km, and the spatial resolution is 1.2 × 18.5 m. An improvement on the azimuth resolution can be achieved using the spotlight mode at the expense of azimuth coverage. The radar antenna beam operating on spotlight mode is steered during the acquisition time from forward to backward, pointing always in the same area on the ground [22]. The spotlight mode of the TerraSAR-X system acquires a standard scene size of 10 × 10 km with a spatial resolution of 1.2 × 1.7 m for single polarization and 1.2 × 3.4 for dual polarization.

1.3 Sea Surface Polarimetric Scattering

This subsection deals with multi-polarization models to describe/predict the backscattering from the sea surface at microwaves.

Over decades, the problem of scattering of electromagnetic waves from natural rough surfaces has been investigated. The rough surface scattering problem plays an important role for the radar remote sensing and its application on extracting information on the observed scene, being of paramount importance for a broad range of operational applications such as sea wind retrieval, soil moisture estimation, sea ice, and oil slick observation [21, 36, 38]. To obtain closed-form solutions is not a trivial task, and therefore, approximation approaches to deal with limiting scattering cases were proposed, i.e., the high-frequency and low-frequency approaches. The analytical high-frequency approach based on the Kirchhoff-tangent approximation is valid for very rough slopes, and it has a good performance in modeling quasi-specular scattering, while it lacks polarization sensitivity. Other very commonly used general analytical approach is the small perturbation model (SPM) based on the low-frequency approximation for small vertical variations. The SPM yields for proper polarization sensitivity (considering the regime where the model is valid);

however, it lacks in accounting specular scattering, multiple scattering effects, and long-scale features in the surface spectrum [84]. Furthermore, the Kirchhoff-tangent approximation and the SPM cannot well model natural rough surfaces since these surfaces have different scales. In this context, in order to overcome the problem of the natural sea surface being a very complicated composite surface, the two-scale approximation assumes that the small roughness rides on top of large fluctuations. The latter model has a good compromise between interpretation, practical implementation, and accuracy issues [24, 35].

First to introduce the three scattering models will be presented in this subsection, the Bragg scattering will be described as well as some general properties of the ocean backscattering. Considering a range of angles of incidence between 20 and 60°, under low-to-moderate wind conditions and the absence of long waves (validity range of the Bragg scattering regime), the SAR sea surface backscattering is primarily due to the Bragg scattering. The incident radiation is backscattered by the wind-generated waves (i.e., capillary or short-wave length waves) of the sea surface, following the relation: $\lambda_B = \lambda_r/2\sin(\theta)$, which says that sea surface roughness scale, λ_B, is comparable with the radar wavelength λ_r. Considering all frequencies, the ocean backscattering decreases with increasing incidence angle while increasing when wind speed increases. The VV-polarized return is higher than the HH one, while the cross-polarized (HV or VH polarization) NRCS is much lower than the co-polarized ones, often being below the noise floor of the SAR sensor [37].

In [36], a scattering model was proposed, which is an extension of the conventional Bragg scattering model, since it includes a roughness-induced rotation symmetric disturbance. According to [36], the great advantages of the model are the ability to describe processes that reduce the degree of polarization of the electromagnetic wave (i.e., depolarization effects) and the capability to describe cross-polarized backscattering. In this framework, it is the possible extension of the Bragg scattering theory to a range of natural surfaces.

Under intermediate incidence angles and low-to-moderate sea-state conditions, the X-Bragg coherency matrix $\boldsymbol{T}_X$ can be predicted introducing a roughness disturbance by rotating the Bragg coherency matrix about an angle β in the plane perpendicular to the scattering plane [36]:

$$\mathbf{T}_X = \begin{pmatrix} C_1 & C_2 \operatorname{sinc}(2\beta_1) & 0 \\ C_2^* \operatorname{sinc}(2\beta_1) & C_3\,(1 + \operatorname{sinc}(4\beta_1)) & 0 \\ 0 & 0 & C_3\,(1 - \operatorname{sinc}(4\beta_1)) \end{pmatrix}. \tag{16}$$

The angle β is an uniformly distributed random variable in the range 0–90°, and its distribution width, β_1, corresponds to the amount of roughness of the sea surface [36].

$$p(\beta) = \begin{cases} \frac{1}{2\beta_1} & |\beta| \leq \beta_1 \\ 0 & \text{elsewhere} \end{cases}. \tag{17}$$

C_1, C_2, and C_3 are combinations of the complex Bragg scattering coefficients:

$$\begin{cases} C_1 = |R_h + R_v|^2 \\ C_2 = (R_h + R_v)\left(R_h^* - R_v^*\right) \\ C_3 = \frac{1}{2}|R_h - R_v|^2 \end{cases}. \tag{18}$$

R_h and R_v are, respectively, the Bragg scattering coefficients perpendicular (V) and parallel (H) to the incidence plane and depend on the local incidence angle, θ, and the relative electric permittivity, ϵ. More details can be found in [36].

Please note that the X-Bragg scattering model does not implement a high depolarizing condition. Thus, this model is not valid for dealing with high depolarizing targets [10].

The electromagnetic scattering model named polarimetric two-scale model (PTSM) [21, 38], as the original TSM, accounts for depolarization effects. However, the former different from the latter one has the advantage to provide closed-form expressions of the elements of the covariance matrix holding large-scale surface slopes. Compared with the X-Bragg model, the PTSM brings improvement when it removes the assumption of a uniform incidence plane rotation β and no variation in the incidence angle. The PTSM was first developed to retrieval soil moisture, and it was expanded to deal with the sea surface scattering purposes in [73, 74].

Considering the PTSM, the ocean can be modeled as being composed of large-scale roughness with slightly roughened, tilted facets whose slope is the same as a smoothed surface at the center of the roughened facet. The small-scale roughness $\delta(x, y)$ is considered as a zero-mean stochastic process with height standard deviation small when compared to the electromagnetic wavelength. Considering $\delta(x, y)$ as a band-limited process, the power spectral density is [32, 38]

$$W(k) = \frac{S_0}{k^{(2+2H_t)}} = s^2 \frac{S_{0n}}{k^{(2+2H_t)}} = s^2 W_n(k), \tag{19}$$

where $k = \sqrt{k_x^2 + k_y^2}$, and k_x, k_y are the Fourier mates of x (azimuth) and y (range), respectively. Via the dimensional facet-size-dependent constant S_{0n}, S_0 is proportional to the roughness variance s^2 [32]. W_n is the normalized power spectral density, and $0 < H_t < 1$ is the Hurst coefficient related to the fractal dimension D by $D = 3 - H_t$. More details about values of D and H_t for the sea surface can be found in [49, 82].

If we consider a sensor illuminating an area at a global incidence angle θ and a field scattered by a single tilted rough facet, the full expression of NRCS can be obtained as [38]

$$\begin{cases} \sigma_{hh}^0 = \frac{4}{\pi} k^4 \cos^4\theta_i s^2 W_n\,(2k\,\sin\theta_i) \\ \times \left| F_h\,(\theta_i)\cos^2\beta_s + F_v\,(\theta_i)\sin^2\beta_s \right|^2 \\ \\ \sigma_{vv}^0 = \frac{4}{\pi} k^4 \cos^4\theta_i s^2 W_n\,(2k\,\sin\theta_i) \\ \times \left| F_v\,(\theta_i)\cos^2\beta_s + F_h\,(\theta_i)\sin^2\beta_s \right|^2 \\ \\ \sigma_{vh}^0 = \sigma_{hv}^0 = \frac{4}{\pi} k^4 \cos^4\theta_i s^2 W_n\,(2k\,\sin\theta_i) \\ \times \left| [F_v\,(\theta_i) - F_h\,(\theta_i)]\,\sin\beta_s\,\cos\beta_s \right|^2 \end{cases}, \tag{20}$$

where F_h and F_v are the Bragg scattering coefficients for horizontal and vertical polarizations, respectively [38]. θ_i is the local incidence angle, and the angle β_s is the rotation of the local incidence plane around the look direction $\hat{k}$ related to the facet slopes. Equation (20) does not hold at near-grazing angles (i.e., $\theta_i \cong \pi/2$) and k values smaller than about $2\pi/L$ (i.e., $\theta_i < \lambda/2L$, where L is the facet linear size).

Considering that the large-scale roughness height variations are larger than the incident radiation wavelength and the facet size is larger than the small-scale roughness correlation length, the returns from different facets are uncorrelated. Within this context, the NRCS from the entire surface can be expressed by averaging that of a single facet over β_s and θ_i. Via a Taylor series expansion, the NRCS expressions of an entire resolution cell are given as follows [38]:

$$\begin{cases} \left\langle \sigma_{hh}^0 \right\rangle_{|a,b} = \frac{4}{\pi} \left[C_{0,0}^{hh} + \left(C_{2,0}^{hh} + 2\frac{\Re\left(C_{0,0}^{hv}\right) - C_{0,0}^{hh}}{\sin^2\theta} + C_{0,2}^{hh} \right) \sigma^2 \right] \\ \left\langle \sigma_{vv}^0 \right\rangle_{|a,b} = \frac{4}{\pi} \left[C_{0,0}^{vv} + \left(C_{2,0}^{vv} + 2\frac{\Re\left(C_{0,0}^{hv}\right) - C_{0,0}^{vv}}{\sin^2\theta} + C_{0,2}^{vv} \right) \sigma^2 \right] \\ \left\langle \sigma_{hv}^0 \right\rangle_{|a,b} = \frac{4}{\pi} \left(C_{0,0}^{hh} + C_{0,0}^{vv} - 2\Re\left(C_{0,0}^{hv}\right) \right) \frac{\sigma^2}{\sin^2\theta} \end{cases}, \tag{21}$$

where $C_{k,n=k}^{pq}$ are series expansion coefficients of the function $(k\,\cos\,(\theta_i))^4\, W F_p F_q^*$ [38]:

$$C_{k,n-k}^{pq} = \frac{1}{n!}\binom{n}{k} \left. \frac{\partial^n \left(W k^4 \cos^4\theta_i F_p F_q^* \right)}{\partial a^k \partial b^{n-k}} \right|_{a=b=0}. \tag{22}$$

Even though the good compromise between interpretation, practical implementation, and accuracy issues [35] associated to the composite model combining the Bragg scattering mechanisms (contribution associated to capillary and short-gravity waves) and local-tilting effects associated to long waves, it is still difficult to obtain a consistent description of the sea surface NRCS over different polarization states and wind and wave conditions as well as over a large range of frequencies and incidence angles [41, 72]. Discrepancies between model and measurement are more significant when considering the sea surface under the influence of surface current straining. In

the literature, the authors have been suggested that that the contribution of surface breaking waves can be considered summing up with the polarized Bragg scattering mechanisms to describe the co-polarized sea surface backscattering, reducing the discrepancies [41, 42].

Other studies analyzed sea surface polarimetric scattering under more complex environmental conditions, i.e., high sea states, the presence of breaking waves and ice caps, internal waves, etc. When dealing with breaking waves, some studies propose that, at intermediate incidence angles, the scattering mechanisms associated to near-breaking events and intermediate-scale breaking waves are characterized as non-polarized, and, therefore, contributing the same for both co-polarized channels [43, 44]. Within this context, according to Kudryavtsev et al. [44], the contribution of breaking wave can be estimated from co-polarized SAR measurements. The model assumes that the sea surface can be described as the sum of a polarized two-scale Bragg sea surface scattering contribution, $\sigma^0_{qq,\mathrm{b}}$, and a NP scattering from breaking waves, σ^0_{wb} [43]:

$$\sigma^0_{qq} = \sigma^0_{qq,\mathrm{b}} + \sigma^0_{\mathrm{wb}}, \tag{23}$$

where q stands for horizontal or vertical polarization. The term σ^0_{wb} can be solved taking into account the co-polarization difference (PD) and the two-scale Bragg scattering polarization ratio (PR) [43]:

$$\sigma^0_{\mathrm{wb}} = \sigma^0_{\mathrm{vv}} - \frac{\sigma^0_{\mathrm{vv}} - \sigma^0_{\mathrm{hh}}}{1 - \sigma^0_{\mathrm{hh,b}}/\sigma^0_{\mathrm{vv,b}}} = \sigma^0_{\mathrm{vv}} - \frac{\mathrm{PD}}{1 - \mathrm{PR}}, \tag{24}$$

where PR is mainly ruled by the local geometry and tilting effects [41, 43]. More details about PR can be found in Kudryavtsev et al. [43, 44].

1.4 Experimental Showcases

In this subsection, some key polarimetric characteristics of the sea surface scattering are shown by means of an experimental showcase.

The polarimetric SAR scene consists of a FP L-band Alos PalSAR-1 image collected over the Tosashimizu coast (Pacific Ocean, Japan) on April 21, 2011. The spatial resolution is 30 × 10 m (range × azimuth), while the incidence angle at mid-range is about 24°. An excerpt of the SAR scene is shown as an RGB image in Fig. 1a, where red, green, and blue colors refer to the modulus of HH-, VV-, and HV-polarized scattering amplitudes, respectively. The dominant yellowish color witnesses that most of the backscattered signal is from the co-polarized channels. To quantitatively show this property, an along-range transect is selected covering a distance of almost 7 km. The behavior of the HH-, VV-, and HV-polarized NRCSs along the transect is shown—in gray, black, and purple lines—in Fig. 1b, where a

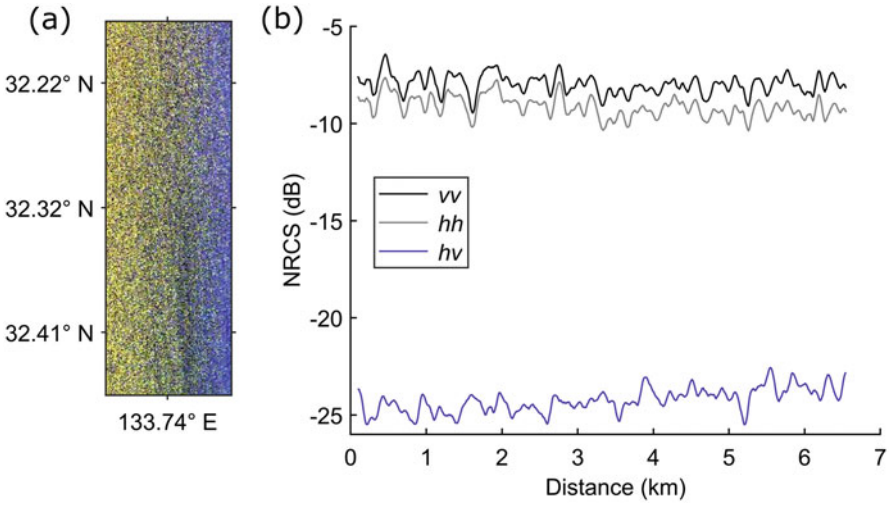

Fig. 1 (**a**) False color RGB (R = $|S_{hh}|$, G = $|S_{vv}|$, B = $|S_{hv}|$) image of a L-band Alos PalSAR-1 SAR scene excerpt collected over sea surface; (**b**) NRCS values (in dB scale) evaluated along a range transect where black, gray, and blue plots refer to vv, hh, and hv polarizations. A smoothing factor of 9 is used to improve visualization

dB scale is used and a 9-pixel-long smoothing window is applied for visualization purposes. It is clear how, over sea surface, co-polarized backscattering dominates over the cross-polarized one, i.e., about 15-dB difference, on average. In addition, it can be noted that the intensity of the VV-polarized backscattering is slightly larger (within 2 dB) than the HH-polarized one. Those properties all come from the peculiar characteristics of the Bragg/tilted-Bragg scattering ruling over sea surface under low-to-moderate wind conditions and in the incidence angle range from about 20 to 60°.

The correlation properties that characterize sea surface polarimetric backscattering can be analyzed using a second-order descriptor, i.e., the 3×3 covariance matrix. To analyze the correlation between the co-polarized channels, the complex-valued element C_{13} must be considered since its phase represents the phase difference between co-polarized channels, i.e., the so-called CPD φ_c. The corresponding probability density function (pdf) is shown in Fig. 2a, where it can be noted that it follows a Gaussian distribution whose width is quite narrow, i.e., less than 10°, witnessing that a large degree of correlation is in place between the HH- and VV-polarized backscattering channels. When dealing the correlation between co- and cross-polarized channels, sea surface satisfies the reflection symmetry property with respect to the line of sight that results in those backscattering channels being uncorrelated. The amplitude of the complex-valued element C_{12}, which is related to the correlation between the HH- and HV-polarized backscattering channels, is shown—in dB scale—as a false color image in Fig. 2b. By visually inspecting Fig. 2b, it can be observed that over sea surface reflection symmetry applies

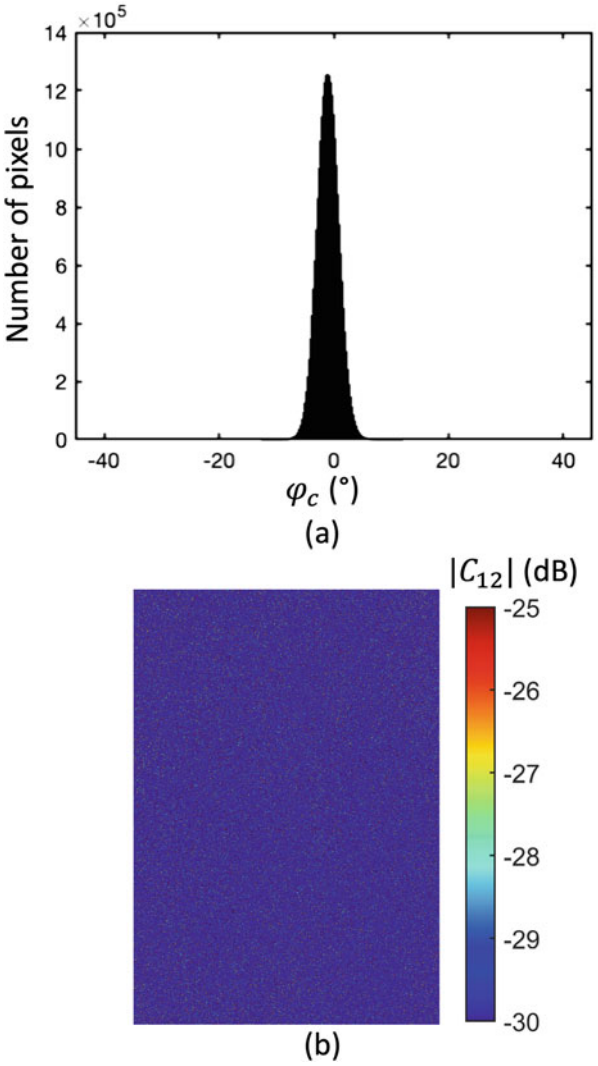

Fig. 2 Behavior of the covariance matrix estimated over sea surface relevant to the Alos PalSAR-1 SAR scene shown in Fig. 1: (**a**) Probability density function relevant to the phase (evaluated in degrees) of C_{13}; (**b**) false color image of the amplitude (in dB scale) of C_{12}

everywhere, i.e., the correlation between HH- and HV-polarized backscattering channels calls for extremely low values (on average, about -34 dB).

To show that the ocean calls for a dominant scattering, i.e., the Bragg/tilted Bragg surface scattering mechanism, the three real and non-negative eigenvalues of the covariance matrix are evaluated, see Fig. 3, where they are normalized with respect to the total backscattered power (namely, the SPAN). As expected, sea surface is

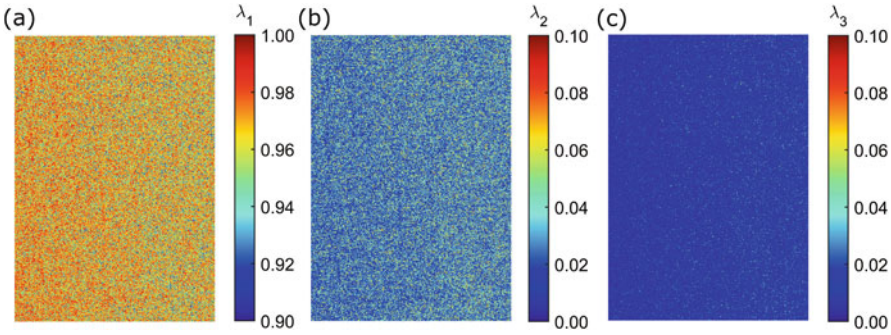

Fig. 3 False color images of the normalized eigenvalues of the coherency matrix evaluated over sea surface relevant to the Alos PalSAR-1 SAR scene shown in Fig. 1: (**a**) λ_1; (**b**) λ_2 and (**c**) λ_3

characterized by λ_1 values larger than 0.9, while λ_2 and λ_3 values lower than 0.1, witnessing that a single scattering mechanism dominates. On average, $\lambda_1 = 0.96$, while the secondary eigenvalues λ_2 and λ_3 are equal to 0.03 and 0.01, respectively.

2 SAR Polarimetry for Sea Oil Spill Observation

In this section, the capability of polSAR satellite measurements to observe oil spills at sea is presented.

Oil pollution has become one of the most frequent and catastrophic marine accidents. There are many sources of marine oil spill pollution, including the natural leakage of hydrocarbons from seabed oil and gas reservoirs, the discharge of industrial wastewater and domestic sewage, the exploitation of offshore oil resources, the blowout accidents of drilling platforms, the rupture of oil pipelines, the leakage and illegal sewage discharge oil tankers, etc. Oil spill mostly occurs in offshore waters, and it will cause huge damage to the marine environment and ecological resources. Crude oil contains a large number of toxic compounds and heavy metals. Once enters the marine ecological cycle, they will first affect the health and safety of low-grade marine plants, then fish, higher mammals, and human beings through the food chain. Oil spill pollution will not only affect the marine traffic, but also cause huge losses to the marine salt industry, offshore water power generation, seawater desalination, and marine aquaculture. To summarize, it will seriously threaten the people's health and economic development of the coastal region.

Remote sensing plays a key role in the early warning, response, and damage assessment of marine oil spill [12]. Compared with optical sensors, SAR has stronger capability of all-day and all-weather observation, which has demonstrated its advantage in operational oil spill observation, especially during adverse weather conditions when oil spill accidents frequently happen. SAR platforms for marine

oil spill observation can be mainly divided into spaceborne and airborne platforms. Spaceborne platforms have the advantage of large coverage and are relatively cost-effective, while airborne platforms have a higher signal-to-noise ratio and are more flexible in repeat observations during emergency responses and can better acquire the drifting and emulsification process of the oil spill.

In ancient Greece, the inhibitory effect of oil film on sea surface fluctuation was recorded in the literature [4]. In ancient navigation, experienced sailors spilled oil to the sea with wind and waves and use the attenuation characteristics of oil film to sea waves to prevent ships from overturning. Italian scientist Maragoni [13] explained this phenomenon theoretically for the first time: substances with different viscosity coefficients on the liquid surface will produce elastic resistance, so as to attenuate the amplitude of surface fluctuation. Therefore, the attenuation of sea oil film is called Marangoni attenuation (damping). Synthetic aperture radar observes backscattering caused by sea surface fluctuations of the sea surface. The oil film on the sea surface will diffuse and form a film with different viscosity coefficients, which attenuate the short-gravity wave and capillary wave, reduce the roughness of the sea surface, weaken the SAR backscattering, and form a dark area in graytones intensity SAR images, as shown in Fig. 4. Therefore, the detectability of sea oil film is closely related to the surface wind field of the sea. If the wind speed is too low, the sea surface will not fluctuate, resulting in extreme low backscattering; and if the wind speed is too high, the oil spill on the sea surface will be dispersed and drifted quickly, making it difficult to be detected. Therefore, the ideal wind speed for SAR sea surface oil spill detection is usually required to be 3–14 m/s [13].

This section is organized as follows: in Sect. 2.1, an overview on the use of polSAR imagery to observe sea oil slicks is presented; in Sect. 2.2, the most relevant polSAR approaches to monitor oil spills at sea are critically reviewed; in Sect. 2.3, an experimental showcase of marine oil spill observation methods using conventional classifiers and convolutional neural networks is demonstrated.

2.1 Overview

Marine oil spills are observed as dark spots on the sea surface. However, many other natural phenomena, such as low wind area, biogenic oil film, rain cell, upwelling, internal wave, atmospheric wave, etc., can also form similar strip or patch-like dark areas, may result in a false alarm. These phenomena are referred as "look-alikes." Therefore, distinguishing oil film between look-alikes has become the key problem of SAR marine oil spill observation. Early SAR oil spill observation mainly relied on single-polarization SAR images. The oil film and look-alikes are classified based on the gray level, texture, and shape information. Therefore, these methods are usually composed of three steps: dark spot detection, feature extraction, and classification [13]. However, oil spill identification with single-polarization SAR data usually requires prior knowledge of the oil film and auxiliary information such as sea surface wind speed. The state of oil spill on the sea surface is influenced by the

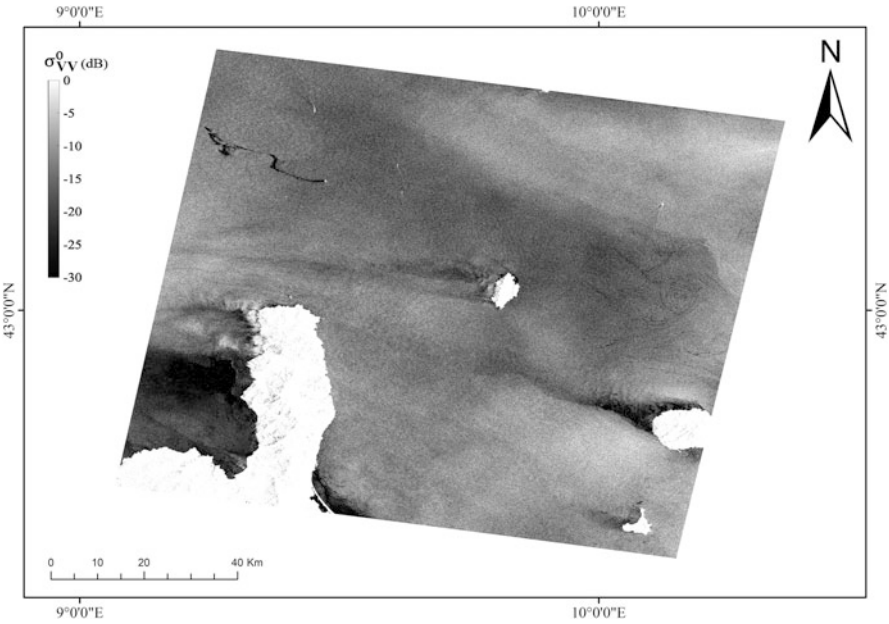

Fig. 4 An excerpt of the VV-polarized NRCS graytone image, shown in dB scale, collected by the C-band Sentinel-1 SAR on October 8, 2018, over a coastal region in the Mediterranean Sea affected by a certified ship-borne oil spill (see the low backscattering slick in the northwestern area). Note that the oil slick is about 30 km long. Several low backscattering regions of different origins (sheltered regions, low wind areas) can also be observed

sea state, which is sometimes very complex. The shape of oil film on the sea surface is related to the oil type and movement of oil source during leakage. Therefore, oil spill observation based on single-polarization SAR data is difficult to implement, and the accuracy cannot be guaranteed. In recent years, oil spill detection based on polSAR data has become a hot research topic. As introduced before, polSAR can obtain detailed backscattering properties of the target and provide more sufficient information for oil spill identification. Study demonstrated that the sea surface covered by mineral oil has distinct scattering mechanisms from the sea surface covered by biological oil film or open water: the Bragg scattering of the sea surface covered by mineral oil is weakened, while the non-Bragg scattering mechanism is enhanced, resulting in obvious depolarization effect. On the other side, the sea surface covered by biological oil film or open water is still dominated by Bragg scattering, with a backscattering of high degree of polarization [6, 56].

Polarization decomposition parameters were considered first for marine oil spill observation. By eigenvalue decomposition of the polarization coherency matrix, polarimetric entropy H and average polarization angle $\bar{\alpha}$ and anisotropy A can be extracted. These parameters are widely used in polSAR-based image analysis. The sea surface covered by biogenic film or open water is dominated by Bragg scattering,

resulting in a small H and $\bar{\alpha}$, while the Bragg scattering mechanism of the mineral oil-covered area is suppressed, making the polarization scattering mechanism more complex, and therefore, H and $\bar{\alpha}$ increase. In [59], the effectiveness of these polarization decomposition features in sea surface oil film detection was confirmed based on SIR-C/X SAR data, while a polarization constant false alarm rate (CFAR) filter for sea surface oil film detection based on these features [57]. In [58], it was first reported that the pedestal height can reflect the degree of depolarization of ground objects. The pedestal height of open water is lower than that of the oil-covered region, which can be used to effectively distinguish mineral oil and its look-alikes. The phase information in polSAR data is closely related to the polarization characteristics of ground objects. In [67], it was first proposed that the co-polarized phase difference (CPD) can be used to effectively distinguish oil spill and biogenic film. The analysis shows that the phase correlation of co-polarized backscattering signals on the sea surface of open water or covered by biogenic slick is high, leading to a phase difference close to 0, while the existence of mineral oil reduces the phase correlation of co-polarized channels and expands the distribution of phase difference. Therefore, the variance of CPD can be used as a powerful feature for oil film classification. In [79], C-band Radarsat-2 and X-band TerraSAR-X data in the North Sea oil spill experiment were analyzed, and the features including H and $\bar{\alpha}$, CPD standard deviation, amplitudes of co-polarized channels, correlation coefficient, and other features were compared on their capability in distinguishing between mineral oil and biogenic oil films.

The NRCS of different polarization channels can be used to classify marine oil films. In the range of medium incidence angles (approximately 20–60°), the radar backscattering of sea surface can be modeled by Bragg scattering. Theoretically, the Bragg scattering on the sea surface is related to the electromagnetic wave number, radar incidence angle, Fresnel coefficient, and sea surface two-dimensional spectrum. The ratio of different polarization backscattering cross sections is only a function of local incidence angle, sea surface slope, and equivalent dielectric coefficient. In [53], it studied the L-, C- and X-band images obtained in the SIR-C/X oil film field experiment, which confirmed this fact. In [63], the tilted Bragg scattering model was used to describe the backscattering of sea surface and oil–water mixture, and Unmanned Aerial Vehicle SAR (UAVSAR) images obtained during the oil spill accident in the Gulf of Mexico were used to retrieve the oil–water mixing ratio. They estimated that the oil–water mixing ratio of the region near the accident site was between 65 and 90%. In [66], the boundary perturbation method was considered to analyze the characteristics of different NRCS of oil-free and biogenic film covered sea surface. The experiments using actual SAR data show that the TSM and Marangoni damping model can better describe the sea surface backscattering cross section under the tilted modulation of large-scale waves. When the range of incidence angles is small, the NRCS of different polarization channels is dominated by the specular scattering component. With the increase of incidence angle, the specular scattering component decreases rapidly, and the radar backscattering cross section is gradually dominated by the contribution of Bragg scattering component. In this case, the small perturbation method (SPM) can be

used for modeling. In [89], an improved backscatter model was proposed based on polarimetric scattering mechanism for marine oil spill observation, which is more in line with the characteristics of oil film covered sea surface, and improved the accuracy of the retrieval of equivalent dielectric constant and other parameters. The NRCS-based analysis methods only rely on the amplitude information of polSAR image; therefore, they can be used in polSAR sensors with incoherent polarimetric imaging modes such as ENVISAT ASAR and CSK. In the dual-polarization mode of these platforms, the signals of different polarization modes are transmitted and received alternately. However, the application of sea surface SPM is greatly limited by the incident angle. At small incidence angles, the specular scattering is too strong, while at large incidence angles the backscattering is too weak. Moreover, the Fresnel coefficient will saturate with the change of sea surface equivalent dielectric constant [36], which affects the accurate retrieval of oil–water mixing ratio. In addition, only when the oil film thickness reaches the order of the skin depth of electromagnetic wave (approximately 1 and 4 mm at C-band and L-band, respectively), its change will have an observable effect on the radar NRCS [85]. However, usually the thickness of oil film is far from the above conditions. In addition, methods based on the NRCS ratio do not make full use of the depolarization effect of sea oil film, which greatly limits its ability to distinguish between mineral oil and its look-alikes.

2.2 PolSAR for Marine Oil Spill Observation

2.2.1 Feature Extraction to Monitor Sea Oil Spills

In this paragraph, some of the most widely used features derived from polSAR imagery to observe marine oil pollution and their expected behavior are summarized. Most of them have been already introduced in Sect. 1.1 and will be interpreted in terms of slick-free and oil slick-covered sea surface, while other features will be first introduced that are specifically proposed for sea oil slick observation purposes. They are as follows:

- Polarimetric entropy
- Degree of polarization
- Ellipticity angle
- Normalized pedestal height
- CPD standard deviation
- Conformity coefficient
- Correlation coefficient
- Coherence coefficient

The intensity of co-polarized channels is frequently used in single-polarization SAR-based oil spill detection algorithms, and therefore, it can be taken as a reference. The VV-polarized NRCS is usually considered due to its higher signal-to-noise ratio (SNR) if compared to the HH-polarized one [54, 55].

The polarimetric entropy, H, assumes values close to 0 over clean sea surface, since the almost completely polarized Bragg scattering dominates, while over oil slick-covered areas, the more random scattering mechanism due to depolarization effects results in larger entropy values, i.e., close to 1. However, for weak-damping slicks as biogenic films, although the backscattering power is still lower than the sea background due to their damping properties, the main scattering mechanism is still Bragg-like [10], i.e., entropy values similar to that of clean sea surface apply.

The degree of polarization, DOP, can be derived from the Stokes vectors of any coherent SAR imaging mode including DP, CP, and FP architectures [77]. When dealing with clean sea surface and weak-damping slicks, the significantly polarized Bragg scattering mechanism results in large DOP values, i.e., close to 1. When sea surface is covered by mineral oil, the latter induces remarkable depolarization effects, and therefore, lower DOP values (approaching 0) are observed.

The ellipticity angle, χ, describes the polarization status of a monochromatic plane electromagnetic wave [17, 77]:

$$\sin(2\chi) = -\frac{g_3}{m g_0}, \tag{25}$$

where g_0 and g_3 represent the first (i.e., the total backscattered power) and the fourth (i.e., the one related to circular polarization) elements of the Stokes vector $\mathbf{g}$, while m is the degree of polarization of the wave. For slick-free sea surface, where Bragg scattering rules, χ is negative, while for oil-covered sea surface, since a more random scattering mechanism is in place, χ is positive [62]. Therefore, χ can be used as a straightforward binary descriptor to distinguish slick-free from oil-covered sea surface [62, 67].

The normalized pedestal height, namely NPH, represents the amount of unpolarized backscattering energy. Hence, for clean sea surface, the almost completely polarized Bragg scattering mechanism results in NPH values close to 0, while for the oil-covered sea surface, much larger NPH values (approaching 1) are expected due to the non-Bragg scattering that reflects the depolarization induced by the mineral oil.

The standard deviation of the CPD, evaluated from φ_c using a sliding window, is an unbiased estimator of the correlation between co-polarized backscattering channels. Over slick-free sea surface, the correlation between co-polarized channels is high, and therefore, a narrow CPD distribution, i.e., a low CPD standard deviation value, is expected [60]. This also applies over weak-damping surfactants. When dealing with mineral oil slicks, the depolarization they induce in scattering mechanism results in a remarkable reduction of the correlation between HH and VV backscattering channels. Accordingly, the pdf of the CPD broadens resulting in a larger standard deviation of φ_c [11, 70].

The conformity coefficient, μ, was first used for soil moisture estimation from CP SAR imagery purposes. When a FP SAR measurement is available, its proxy is defined as [93]:

$$\mu \cong \frac{2\left(\mathrm{Re}\left(S_{hh}S_{vv}^{*}\right) - |S_{hv}|^{2}\right)}{|S_{hh}|^{2} + 2\,|S_{hv}|^{2} + |S_{vv}|^{2}}. \tag{26}$$

The conformity coefficient μ evaluates whether surface scattering is dominant among all the elementary scattering mechanisms. Over a slick-free sea surface, Bragg scattering results in a very small cross-polarized backscattering power while calling for high correlation between co-polarized channels, i.e., $\mathrm{Re}\left(S_{hh}S_{vv}^{*}\right) > |S_{hv}|^{2}$; hence, μ is positive. Over oil-covered sea surface, as non-Bragg surface scattering is in place, the co-polarized correlation is lower, while the cross-polarized backscattering component keeps almost the same, i.e., it is very likely to have $\mathrm{Re}\left(S_{hh}S_{vv}^{*}\right) < |S_{hv}|^{2}$, thus resulting in negative μ values. Considering weak-damping slicks, since Bragg scattering is still dominant, positive μ values are expected. Under this rationale, conformity coefficients can be used to effectively distinguish crude oil from biogenic slicks without any need of external thresholding methods.

The correlation and coherency coefficients can be derived from the coherence matrix as follows [78]:

$$\rho_{c} = \left|\frac{\left\langle S_{hh}S_{vv}^{*}\right\rangle}{\left\langle S_{hh}^{2}\right\rangle\left\langle S_{vv}^{2}\right\rangle}\right| \quad , \quad C_{c} = \frac{|\langle T_{12}\rangle|}{\sqrt{\langle T_{11}\rangle\langle T_{22}\rangle}}. \tag{27}$$

They both range between 0 and 1. Over a slick-free sea surface, the co-polarized channels are highly correlated, so they are expected to be very close to 1, while over oil-covered sea surface, a much lower co-polarized correlation is expected; thus they are both approaching 0.

The general behavior of the above introduced set of polarimetric over slick-free and slick-covered sea surface is summarized in Table 2.

Table 2 Main polSAR features used for sea oil spill monitoring. Note that the VV-polarized NRCS is also listed as a reference

PolSAR feature	Sea surface	Mineral oil—strong damping	Biogenic slick—weak damping
H	Lowest	High	Low
DOP	High	Low	High
χ	Negative	Positive	Negative
NPH	Lowest	High	Low
σ_{φ_c}	Lowest	High	Low
μ	Positive	Negative	Positive
ρ_c	Highest	Low	High
C_c	Highest	Low	High
σ_{vv}^{0}	High	Lowest	High

2.2.2 CP SAR Architectures

The FP spaceborne SAR system alternately transmits horizontal and vertical polarization signals. Therefore, the pulse repetition rate of linear frequency modulation signal is twice that of single-polarization SAR systems, resulting in halved swath width, which lead to range ambiguity effect and increased system power requirements [14]. In addition, the large system complexity and data volume also increase the cost of FP SAR systems. In order to overcome such issues, the CP architectures were proposed. The CP SAR systems can obtain part of the polarization characteristics of the observed targets without reducing the width of the swath [75]. At present, it has achieved promising results in land use classification, biomass estimation, soil moisture retrieval, and several marine applications [1, 47]. For the application of maritime monitoring, the revisit time is a very important technical index, so CP SAR has become a hot research field for marine oil spill observation [61]. The commonly used CP SAR imaging modes in oil spill detection mainly include $\pi/2$, also known as circular polarization transmitting, linear polarization receiving (CTLR), or hybrid polarization mode, and $\pi/4$ or slant linear modes. These two modes transmit circular polarized or 45° linear polarized signals, respectively, and receive horizontal and vertical polarization signals simultaneously. The target scattering vectors $\mathbf{k}$ of those CP SAR sensors are

$$\mathbf{k}_{\frac{\pi}{2}} = \frac{1}{\sqrt{2}} \begin{pmatrix} S_{hh} - jS_{vv} \\ S_{vh} - jS_{vv} \end{pmatrix} \quad , \quad \mathbf{k}_{\frac{\pi}{4}} = \frac{1}{\sqrt{2}} \begin{pmatrix} S_{hh} + S_{hv} \\ S_{vh} + S_{vv} \end{pmatrix}. \tag{28}$$

One way for processing CP SAR data is to reconstruct the pseudo-quad-polarization covariance matrix from the compact polarization scattering vector by using iterative algorithms [65, 81] and then use feature extraction methods for FP SAR data. In [86], a CP SAR image reconstruction algorithm based on polarization decomposition was proposed and applied to ship detection. In [18], an empirical model was exploited to estimate the constant parameter N in the range of incidence angles to improve the reconstruction accuracy. The advantage of feature extraction methods based on pseudo-quad-polarization reconstruction is that the analysis methods for fully polarized modes can be directly used. However, for these methods, assumptions of backscattering characteristics are required, which do not always hold for the sea surface. Therefore, sometimes there is a large deviation between the reconstructed pseudo-quad-polarization covariance matrix and the real data. In [52], the backscattering characteristics of the sea surface were analyzed through the statistical analysis of FP UAVSAR data and put forward an improved hypothetical equation, which obtained a better reconstruction performance.

Another way is to analyze the scattering vector of CP SAR data and extract the features directly. The Stokes vector of the radar signal can be obtained from the CP scattering vector, so as to further calculate the degree of polarization m and relative phase δ, wave polarization entropy H_w, ellipticity angle χ, and average polarization angle $\bar{\alpha}_w$. In [50], it was found that the sign of δ can distinguish different sea surface scattering mechanisms: for sea surface region δ is close to

90°, and for oil film covered area δ is negative, making it a binary classification index. Through the image analysis of mineral oil naturally leaked from Radarsat-2 sea surface, in [51], it was also found that compared with the clean sea surface, the m value of the oil film covered area is significantly reduced, indicating that the depolarization effect is obvious and the ellipticity angle is high, and the opposite sign of χ indicates that the scattering mechanism is no longer Bragg scattering. Conformity coefficient μ was first used for soil moisture estimation based on CP SAR. It can effectively distinguish single surface scattering, double-bounce scattering, and volume scattering [93]. The μ extracted from FP and $\pi/4$ CP SAR images have been proven to have a very good ability to distinguish between mineral oil film and biogenic look-alikes. It is positive on the open water and negative on the mineral oil film, so can be used as a logic classifier for sea surface oil spill detection. Based on the extended Bragg scattering model, in [88], a new method was proposed to extract features from the Stokes matrix of CP SAR, and its performance in distinguishing sea oil spill from biogenic slicks and low-wind-speed area was confirmed through experiments. In [91], various features extracted from $\pi/2$ CP SAR mode were analyzed by using the quad-pol reconstruction and direct feature extraction, respectively. It was found that the two kinds of feature extraction methods have their own advantages over each other, and the marine oil spill classification performance of CP SAR is close to the FP SAR mode. In [90], performance of features extracted from DP, CP, and FP SAR imaging modes was investigated. It was found that the classification accuracy will not always increase with the number of features, indicating that there is a large amount of complementary information between polarimetric features, which highlights the importance of feature selection and optimization. In [45], actual $\pi/2$ CP mode RISAT-1 SAR data were used for the first time during an oil spill experiment carried out on Norwegian waters.

Comparative studies have been made on CP SAR modes. The $\pi/2$ CP SAR mode has the advantages of convenient polarization calibration, polarization channel power balance, not dependent on the direction of ground objects and not easily affected by the Faraday rotation effect of the ionosphere [81]. However, it is difficult to transmit an ideal circular polarized signal in engineering practice. The $\pi/4$ CP SAR mode is relatively easier to implement, but there is a 3 dB loss of received power due to the mismatch between the transmitting and receiving polarimetric channels. In [8, 9], the variability of CP SAR features under different incident angles was investigated through experiments on Alos-1, Alos-2, and Radarsat-2 spaceborne SAR images. The ability of CP SAR modes in distinguishing oil film and weak-damping look-alikes was verified, and the differences between polarimetric characteristics obtained under various CP and FP SAR systems were discussed.

2.2.3 Challenges and Research Trend

Controversy still exists on the polarimetric scattering mechanism of marine oil spill. There are beliefs that the increase of non-Bragg scattering component the

SAR image of an oil spill area is probably not mainly caused by the sea surface physical process, but thermal noise of the radar system [40]. In [26], the effects of both additive and multiplicative noise were also analyzed on L-, C- and X-band SAR data. The depolarization effect observed over oil spills in spaceborne SAR imagery was mainly attributed to the additive noise of the SAR sensor. It was also claimed that the non-Bragg scattering occurring over slick-covered sea areas is likely due to a misinterpretation of SAR images collected a too low SNR [19, 26]. However, it has to be noted that the polarimetric backscattering mechanism of oil film is related to many factors including wind speed and the amount of oil leakage. In [10], a sensitivity analysis on the standard deviation of the CPD for marine oil spill observation was undertaken and confirmed that noise plays a role in broadening the distribution of CPD, especially at large incidence angles. The authors claimed that the depolarization is both induced by the noise and oil film. At lower incidence angle, the scene induced depolarization is dominant, while at larger incidence angle, the noise floor plays a more important role. In other words, together with the depolarization inherently introduced by oil, an additional depolarization contribution is due to noisy oil samples. Nonetheless, from the aspect of oil spill detection, this is a good point since the heavier the oil depolarization, the larger the separability with the polarized sea scattering is. On the other side, it makes the classification/characterization/oil parameter retrieval made on "noisy" oil samples unreliable.

The retrieval of the detailed properties of oil slicks and their evolving/drifting under marine environment has been a hot research topic, which received growing attention in recent years. In [74], the use of PTSM is proposed to retrieve the dielectric parameters of oil slick from the polSAR imagery. In [25], FP and CTLR SAR features were analyzed to observe evolving oil spills. They also developed and explored new quantitative and semi-automated methods for analyzing oil slick evolution using a time series of L-band polSAR images with short repeat time [27]. In [39], an analysis on newly formed sea ice distinction near the oil platform in the Pechora Sea was performed using Radarsat-2 polSAR observations. These studies demonstrated the valuable role played by polarimetric information.

With the increase of available polSAR data, deep-learning-based methods have shown great potential in improving the accuracy of marine oil spill classification. As data-driven pattern recognition methods, deep-learning-based algorithms can better exploit the semantic and contextual information within high-resolution SAR images without the need of prior knowledge. Chen et al. [15] used stacked auto-encoder (SAE) and deep believe neural network (DBN) to extract and optimize polSAR features. An oil spill detection method exploiting convolutional neural network and image stretching based on superpixel was proposed in [27], where the effectiveness of the approach was successfully demonstrated on Sentinel-1 DP SAR data. In [46], different parameters were exploited with sensitivity to the dielectric constant and ocean wave damping properties and used CNNs for learning nonlinear features, shapes, and textural and statistical patterns, in order to obtain significant classification accuracy. In [80], a novel oil spill identification method based on multi-layer deep feature extraction by CNN was proposed. These studies show that

compared with traditional supervised learning methods, the deep-learning-based methods with unsupervised pre-training can improve the accuracy of sea surface oil film detection, especially when the training samples are limited.

2.3 Experimental Showcase

2.3.1 SAR Polarimetry for Sea Oil Spill Observation: Conventional Classifiers

This showcase is addressed by means of a C-band FP SAR scene collected at C-band from the Radarsat-2 mission. The image was obtained in the North Sea area near Norway, which was obtained from an oil-on-water field experiment [79]. We selected a sub-region with 2000 × 2000 pixels from the original SAR image that contains clean sea surface and three types of oil films, including mineral oil film, emulsified oil film, and biogenic film. Since the emulsified oil represents an intermediate behavior between crude oil film and clean sea surface, whose polarimetric features are not typical, the classification of emulsified oil film is not considered in this chapter. Figure 5 shows the Pauli RGB image and artificial sampling labels.

In this section, support vector machine (SVM) is used as a representative of classic supervised classifier for its high performance in remote sensing applications. SVM relies on the maximization of the classification margin based on the principle of structural risk minimization. Its good generalization ability is obtained by

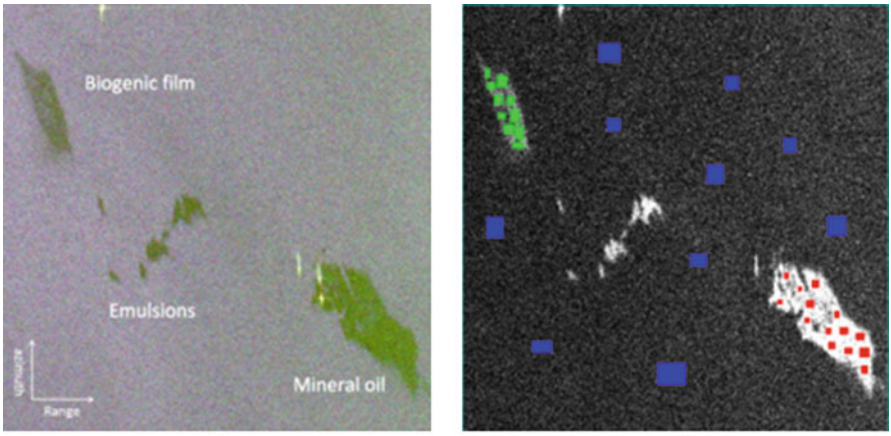

Fig. 5 Experimental showcase: (**a**) false color Pauli RGB image and (**b**) VV-polarized NRCS graytone image with sampling labels (blue: seawater; red: mineral oil; green: biogenic film)

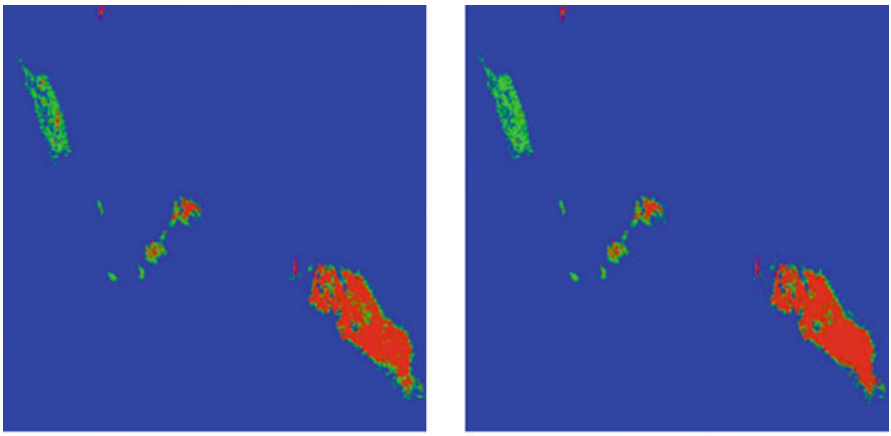

Fig. 6 Classification result relevant to: (**a**) the first and (**b**) the second feature sets

Table 3 Confusion matrix derived from the first feature set. OA = 91.94%

Ground truth (pixels)			
	Mineral oil	Biogenic film	Sea
Mineral oil	12,862	846	24
Biogenic slick	1106	13,324	1039
Sea	20	4945	64,867

Table 4 Confusion matrix derived from the second feature set. OA = 95.60%

Ground truth (pixels)			
	Mineral oil	Biogenic film	Sea
Mineral oil	13,564	728	17
Biogenic film	413	16,182	983
Sea	11	2205	64,930

constructing a lower Vapnik–Chervonenkis dimension function set in a high-dimensional space.

Pixel-level samples of mineral oil, biogenic film, and clean seawater were selected in the region of interest. Two feature sets are generated in the experiment. The first feature set consists of the 9 independent real-valued elements of the coherency matrix, while the second feature set consists—in addition to the first feature set—of the 10 polarimetric features listed in Table 2. The multi-layer perceptron kernel function is used as the kernel function of the SVM. The classification maps are shown in Fig. 6, while the corresponding confusion matrices are listed in Tables 3 and 4, respectively.

By analyzing the results listed in Tables 3 and 4, it can be seen that the classification accuracy is improved by 3.7% when adding the pre-defined polarimetric

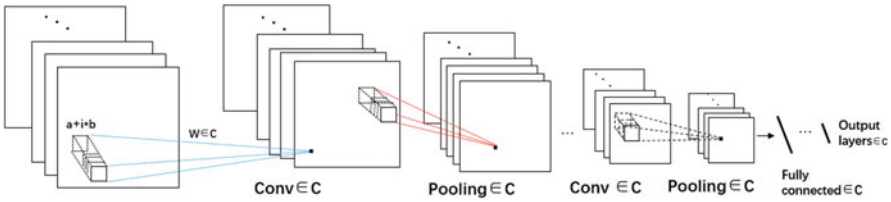

Fig. 7 Network structure of CVCNN[83]

features. The significant improvement in accuracy is mainly due to the reduced mis-classification rate between biogenic film and mineral oil, manifesting that the artificially defined polSAR features based on scattering mechanism carry key information for distinguishing mineral oil spill and its biogenic look-alikes.

2.3.2 SAR Polarimetry for Sea Oil Spill Observation: Convolutional Neural Network Classifiers

In the fields of image classification and target detection, deep learning models represented by the convolutional neural network have shown superior performance. Several studies were proposed to classify polSAR images using CNN, but since these methods take real-valued data as the input, the phase information in polSAR images could not be fully utilized. Therefore, [83] presented a complex-valued convolutional neural network (CVCNN) with complex-valued data as its input, which is of great significance for processing images containing complex-valued information. Trabelsi et al. [83] applied CVCNN to the classification of ground objects in polSAR images and achieved good results. In this chapter, the CVCNN is adjusted for marine oil spill detection tasks, and its performance is compared with real-valued convolutional neural network (RVCNN) based on different feature sets as the input. The network structure of CVCNN [83] used in this chapter is shown in Fig. 7, including input layer, convolutional layers, pooling layers, fully connected layer, and output layer. Different to the general CNNs, the weight and bias of CVCNN, including the input and output of all layers, are fully defined in the complex domain.

In CVCNN, the model input is a complex number, then its real part A and imaginary part B are expressed as logically different real numbers, and complex operation is simulated internally using real number algorithms. In the convolutional layer, complex convolution operation can be expressed as

$$\boldsymbol{W} \times \mathbf{h} = \left(\boldsymbol{A} \times x - \boldsymbol{B}^{*} y\right) + j\left(\boldsymbol{B}^{*} x + \boldsymbol{A} \times y\right) \tag{29}$$

$$\begin{bmatrix} \mathrm{Re}(\boldsymbol{W} \times \mathbf{h}) \\ \mathrm{Im}(\boldsymbol{W} \times \mathbf{h}) \end{bmatrix} = \begin{bmatrix} \boldsymbol{A} & -\boldsymbol{B} \\ \boldsymbol{B} & \boldsymbol{A} \end{bmatrix}, \tag{30}$$

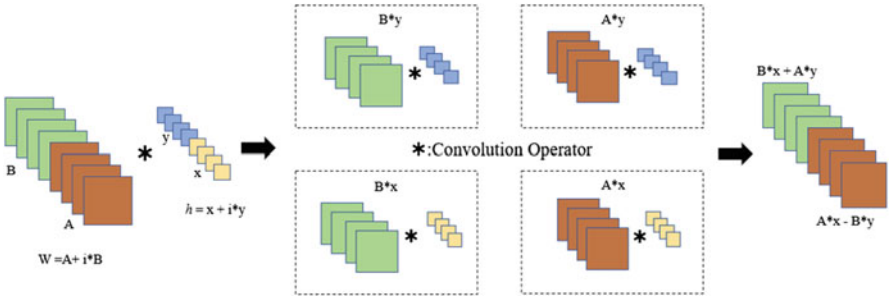

Fig. 8 Complex convolutional operation process

where $\mathbf{h}$ is the input of complex-valued vector network, i.e., $\mathbf{h} = x + jy$; $\boldsymbol{W}$ is the weight complex matrix, i.e., $\boldsymbol{W} = \boldsymbol{A} + j\boldsymbol{B}$. Re(·) and Im(·) mean real and imaginary parts, respectively. For a more intuitive representation, the complex convolutional operation process is shown in Fig. 8.

Accordingly, the ComplexReLU (CReLU) function is used as the complex activation function of CVCNN, whose operation process is as follows:

The weight and bias are initialized by means of random initialization. The complex backpropagation algorithm adopts stochastic gradient descent (SGD) to optimize the real part and imaginary part.

Figure 9 shows the structure of the proposed CVCNN and RVCNN for comparison. It should be noted that all the off-diagonal elements of the coherency matrix are complex-valued data, which contain important phase information. Therefore, T_{11}, T_{12}, T_{13}, T_{22}, T_{23}, and T_{33} are input into the classification network as six channels. While for RVCNN, the input is real-valued T_{11}, T_{22}, T_{33}, and the real part and imaginary part of T_{12}, T_{13}, and T_{23}, so nine channels are taken as the input. To avoid the interference by the network layer structure, the network layer parameters of the two networks are kept consistent. Finally, the network outputs the classification result of three types of targets, namely mineral oil slick, biogenic oil film, and seawater.

The same two feature sets are also applied in the oil spill classification experiments based on real-valued and complex-valued convolutional neural networks, respectively. For CNN, each pixel in the image is represented by a local patch defined by a neighborhood window. In this chapter, a 12×12 sliding window was used to obtain the data input of the CNN. Therefore, the classification model captures not only the polarimetric characteristics but also the spatial and texture patterns surrounding the center pixel that to be classified.

For the first feature set, T_{11}, T_{12}, T_{13}, T_{22}, T_{23}, and T_{33} are directly input into the CVCNN as 6 channels, while the real-valued T_{11}, T_{22}, T_{33}, and the real part and imaginary part of T_{12}, T_{13}, and T_{23} are input into the RVCNN as 9 channels, respectively. Then for the second feature set, the previously introduced polarimetric features are also input into RVCNN and CVCNN as supplementary feature dimensions.

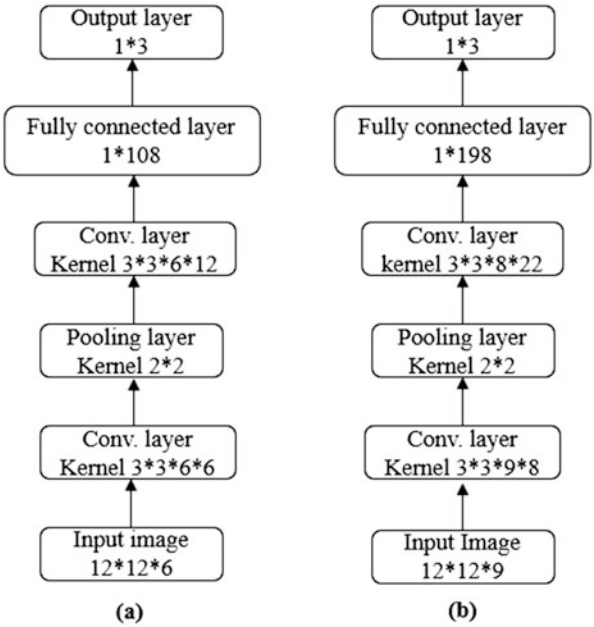

Fig. 9 Flowchart of: (**a**) CVCNN and (**b**) RVCNN

It can be observed from Fig. 10 and Tables 5 and 6 that, based on the elements only on T matrix, CVCNN has better classification performance than RVCNN by 0.3494%. The main reason is that the proposed RVCNN can better take advantage of the phase information contained in the polSAR data, which greatly helps to distinguish mineral oil and biogenic films. As shown in Fig. 11 and Tables 7 and 8, when the pre-defined polSAR features are introduced, the oil spill classification accuracy derived by RVCNN- and CVCNN-based methods improved by 0.9032% and 0.6736%, respectively, resulting in the classification accuracy derived by CVCNN still slightly higher than RVCNN. The results demonstrated that these polarimetric SAR features have relatively larger help to RVCNN-based model, by providing key polarimetric information hidden in the phase information of the complex backscattering coefficients. The experimental results demonstrated that the introduced SAR features provide key polarimetric information for improving the performance of oil spill classification. It is preliminarily shown that the CVCNN has the overall best performance for its ability of extracting both special and polarimetric information from polSAR data. Theoretically, deep-learning-based methods have higher potential given a larger number of training samples. Its advantage on dealing with complex function fitting problems may provide greater help in oil spill observation tasks under more complex environments and various oil type conditions.

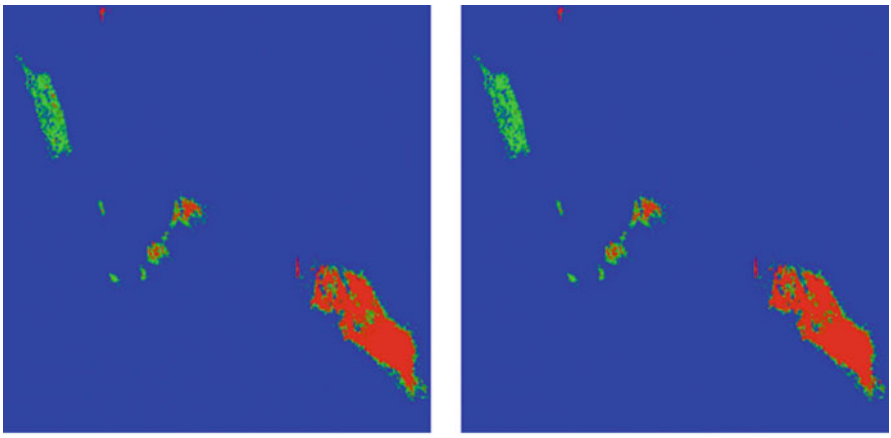

Fig. 10 Classification results obtained from the first feature set using (**a**) RVCNN and (**b**) CVCNN

Table 5 Confusion matrix derived from the first feature set by RVCNN. OA = 95.97%

Ground truth (pixels)			
	Mineral oil	Biogenic film	Sea
Mineral oil	13,602	426	9
Biogenic film	373	16,940	1422
Sea	13	1749	64,499

Table 6 Confusion matrix derived from the first feature set by CVCNN. OA = 96.32%

Ground truth (pixels)			
	Mineral oil	Biogenic film	Sea
Mineral oil	13,774	264	11
Biogenic film	197	17,219	1525
Sea	17	1632	64,394

3 SAR Polarimetry for Shoreline Monitoring

In this section, the capability of polSAR satellite measurements to monitor shorelines and to support coastal area management is provided.

Coastal areas are, worldwide, economic and natural resources of extraordinary value that, being often fragile and dynamic environments mostly largely urbanized, are particularly vulnerable to natural and anthropogenic hazards. Although in 2011 it was estimated that the world coastline length is around 1 million kilometers [5], this value tends to rapidly change over time due to natural phenomena, e.g., sea-level rise, erosion and sedimentation, and human-induced processes, e.g., urbanization and deforestation. In addition to the coastal area vulnerability issue, the fast growth

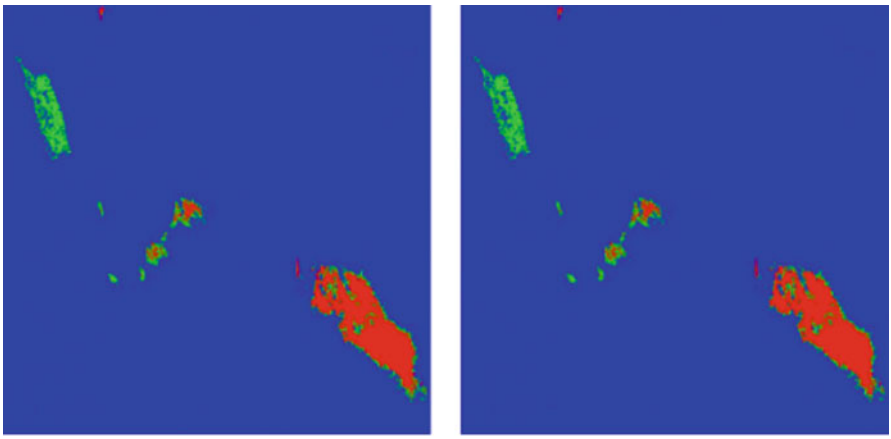

Fig. 11 Classification results obtained from the second feature set using (**a**) RVCNN and (**b**) CVCNN

Table 7 Confusion matrix derived from the second feature set by RVCNN. OA = 96.87%

Ground truth (pixels)			
	Mineral oil	Biogenic film	Sea
Mineral oil	13,729	198	32
Biogenic film	238	17,153	845
Sea	21	1764	65,053

Table 8 Confusion matrix derived from the second feature set by CVCNN. OA = 96.99%

Ground truth (pixels)			
	Mineral oil	Biogenic film	Sea
Mineral oil	13,811	197	18
Biogenic film	161	17,241	910
Sea	16	1677	65,002

of the coastal population density and the increase in economic assets and critical infrastructures in coastal areas pose a serious threat to human society. Hence, accurate and systematic observation of the coasts over time and, therefore, methods to predict the coastal evolution play a fundamental role in coastal zone management. Indeed, effective operational service for coastal areas monitoring is a key topic for local authorities that face the aforementioned threats for the stability of land and the safety of people they are responsible for. Within this context, microwave remote sensing plays a fundamental role in coastal area monitoring. In particular, SAR sensors, due to all-day and almost all-weather acquisitions, together with a wide area coverage and a fine spatial resolution, can be very useful for coastal area monitoring purposes [71].

This section is organized as follows: in Sect. 3.1, the most up-to-date advancements in coastline extraction from polSAR imagery is presented; the methodology to process polSAR imagery to extract the coastline is detailed in Sect. 3.2, while experimental results are showcased and discussed in Sect. 3.3.

3.1 State-of-the-Art

In this section, an overview of the studies that deal with shoreline monitoring using polSAR measurement is presented. In [87], the enhancement of the land/sea contrast is undertaken using polarimetric methods. Experimental results, undertaken on C-band Convair airborne polSAR data, show that the polarimetric combination outperforms single-polarization ones. The radar frequency dependence is discussed in [64], where results showed that higher frequency (C- or X-band) provides the best coastline localization. In [3], an analysis of the polarimetric channels with respect to the angle of incidence is undertaken. Experimental results show that, at low AOI ($<30°$), the cross-polarized channel performs better than the co-polarized ones, while at higher AOI, no polarization dependence is exhibited. Co-polarized DP CSK SAR data, collected using the incoherent PingPong Stripmap mode, are successfully exploited to extract coastlines by Nunziata et al. [68]. Coastline extraction in an intertidal flat area is addressed in [23], where experimental results, obtained using CSK DP SAR scenes, pointed out that the extraction accuracy decrease in the case of water within the intertidal flat. In [7], a multi-polarization analysis of coastline extraction is undertaken using X-band single-polarization CSK SAR data. Results show that the performance of cross-polarized channels depends on the incidence angle while showing a small sensitivity to sea-state conditions. Conversely, co-polarized channels show a remarkable sensitivity to sea-state conditions. In addition, it is also pointed out that sandy coasts are badly detected due to very limited sand/sea contrast. In [69], the DP metric, based on the correlation between co- and cross-polarized channels, is exploited to enhance the contrast between sea and land. Results, obtained processing DP C—and X-band SAR data, demonstrate the soundness of the proposed approach for coastline extraction purposes. The FP information is exploited in [29]. In this chapter, the surface and the volume component obtained from the Freeman–Durden decomposition are used to enhance the discrimination between the sea and a challenging scenario that includes sandy beaches. Experimental results show that the surface component provides the best performance in terms of accuracy in detecting the sandy beach. In [20], shoreline rotation has been analyzed to provide a better understanding of the morphodynamic processes of natural embayed beaches. In [30], a two-year time series of multi-polarization Sentinel-1 SAR imagery is exploited to analyze the changes in the water-covered area of the Monte Cotugno (Italy) reservoir. Experimental results, verified using independent in situ measurements, demonstrate, first, that Sentinel-1 time series can be successfully used to support the smart water management of reservoirs, and second, multi-polarization feature outperforms SP ones in terms of

accuracy of the extracted waterline profile. In [31], the joint use of non-local speckle filtering and multi-polarization features is applied on a very challenging scenario that includes different habitats such as wetland, salt marshes, sand dunes, sand banks, mudflats, and intertidal flats. Experimental results, undertaken on C-band FP Radarsat-2 SAR imagery, show that the joint combination of non-local speckle filters and dual-polarimetric information provides the best accuracy.

3.2 Methodology

In this section, the methodology developed to address coastline extraction, depicted in the block diagram of Fig. 12, is discussed. Coastline extraction is basically based on two steps. The first step relies on the enhancement of the separation between sea and land, and it is addressed by exploiting the polarimetric information. Following the block diagram of Fig. 12, first, a pre-processing of the polSAR imagery is undertaken that includes calibration, spatial multilooking to reduce the speckle noise using a window size $N \times N$, spatial geocoding, and subset generation that includes the region of interest. Then, a multi-polarization feature is introduced that was found to improve the degree of scattering separability between land and sea [69]. This parameter, labeled as r, consists of average product between co- and cross-polarized backscattering amplitudes:

$$r = \langle |S_{xx}||S_{xy}| \rangle. \tag{31}$$

Accordingly, low r values are expected over sea surface due to negligible cross-polarized backscattering, while larger r values are expected over land—depending on coastal morphology, e.g., sand, rocks, vegetation, urban, ice—due to the significant contribution of both co- and cross-polarized backscattering.

To generate a binary image where land and sea are clearly distinguished, a CFAR algorithm is used to obtain a global threshold. CFAR is an adaptive algorithm used in radar systems to detect target returns against a background of clutter [76].

When dealing with r, since it describes the scattering from a first-order Bragg scattering surface, it is expected to be Rayleigh distributed over the sea surface. Hence, according to [69], the relationship between the detection threshold th and the probability of false alarm P_{fa} is given by

$$P_{fa} = \int_{th}^{\infty} \frac{r}{\sigma^2} e^{\frac{-r^2}{2\sigma^2}} dr \quad th = \sigma \sqrt{-2ln(P_{fa})}, \tag{32}$$

where σ is the standard deviation of the Rayleigh distribution. According to Eq. (32), for a given P_{fa}, a global threshold th can be obtained. In this test case, a P_{fa} equal to 10^{-6} is used.

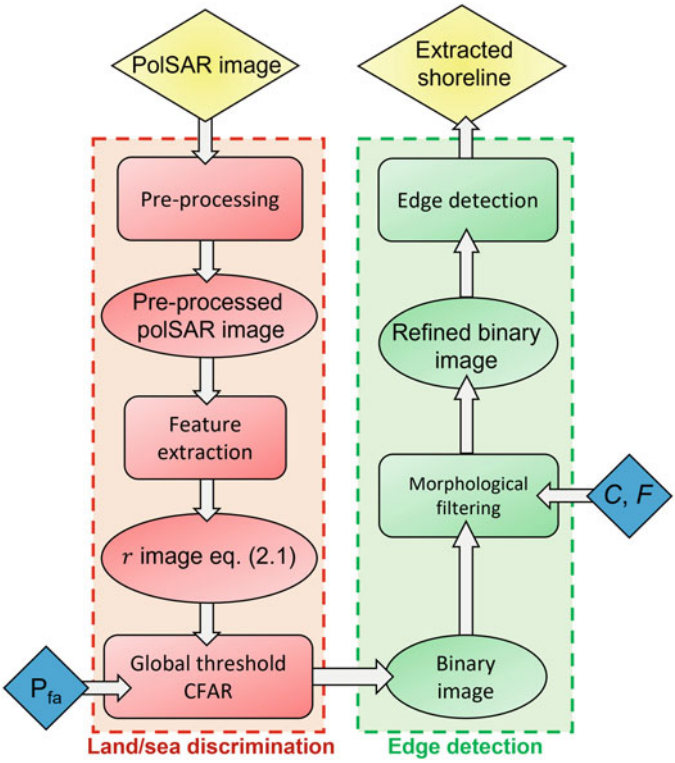

Fig. 12 Block diagram of shoreline extraction

The second step relies on the extraction of continuous coastlines [29], see the edge detection block in Fig. 12. First, the global threshold th obtained from the CFAR approach is used to generate a binary image that separates land from the sea according to the decision rule $r \geq th$.

Then, to refine the binary image by removing artifacts and filling holes, morphological filtering is addressed. The artifacts are removed using an image processing operation called area opening that removes all connected pixels that have fewer than C pixels, while the holes are filled using an image filtering that replicates the pixels inside a hole of $C \times C$ pixels. Finally, to extract the one-pixel continuous coastline from the binary output, the conventional Sobel edge detector is used [2], which is an image processing technique for finding the boundaries of objects within images detecting discontinuities in brightness. Once edges are extracted from the binary output, the one-pixel continuous coastline is obtained.

3.3 Experimental Showcase

In this section, a showcase is discussed to show the benefits of polarimetric methods in monitoring coastal areas. The SAR data set consists of two C-band DP (VV+VH) Interferometric Wide (IW) ESA Sentinel-1 collected over the Calabria coast, in Italy. The area includes the towns of Cetraro Marina and Marina di Belmonte, two municipalities of Cosenza, an Italian town of the region Calabria, on July 11, 2016 and July 3, 2021 in descending mode with an AOI around 46°. Wind conditions, estimated from the cross-polarized channel according to [92], call for low-to-moderate wind (5.1 m/s and 4.7 m/s, respectively). A square pixel whose spacing is 14 m is considered. The false color SAR data collected on July 11, 2016 is ground-projected and shown as an image in Fig. 13a, where red, green, and blue channels stand for VV, VH, and VV/VH power ratios. To reduce the speckle noise in the SAR image, a boxcar filter with a window size 9×9 is applied. The RGB speckle filtered image is shown in Fig. 13b. The metric r (31) is evaluated using $N = 9$, and the output is shown in false color in Fig. 13c. The r image clearly shows that land and sea are well separated, with sea surface exhibiting a very homogeneous behavior in terms of r values. To clearly separate land from the sea, a binary image is generated where the global threshold is obtained using the CFAR approach described in Sect. 3.2 with a probability of false alarm, $P_{fa} = 10^{-6}$. To refine the image, i.e., to fill in the hole and to filter out the isolated pixels, morphological filtering is applied, with $F = 100$ and $C = 9$. The resulting binary image is shown in Fig. 13d, where sea and land are clearly separated. To extract the coastline in a simple and effective way, an edge detection approach based on the Sobel operator is applied on the binary image of Fig. 13d. The extracted coastline, superimposed on the SAR image, is shown in red in Fig. 13e. It can be noted that the coastline extracted well fits the SAR image coastal profile. The same processing flowchart is applied on the SAR scene relevant to July 3, 2021.

To analyze the changes that occurred on the coast from 2016 to 2021, two areas are considered (see the yellow and green boxes of Fig. 13e). Results are shown in Fig. 14, where the waterlines extracted are superimposed to the VV-polarized NRCS SAR image. The yellow and blue lines refer to the coast in 2016 and 2021, respectively, while the white line refers to an area where the overlapping occurs. The first area, enclosed in the yellow box of Fig. 13e, refers to the coast of Cetraro Marina, an area strongly affected by coastal erosion as reported in the European Atlas of the Seas [28]. By visually inspecting Fig. 14a, it can be noted that the extracted coastline rarely calls for white color, witnessing a non-overlapping between coastlines extracted in 2016 and 2021. A comparison between the yellow and blue lines shows a remarkable loss of coastal area, indicating significant coastal erosion occurred in this time frame (2016–2021). The changes in terms of the coastal area between 2016 and 2021 are estimated from the related binary imagery considering the actual pixel spacing. A net erosion of 11.2×10^4 m^2 is estimated, i.e., five years resulted in a degradation loss of an area that is about 21 times larger than a regular American football pitch.

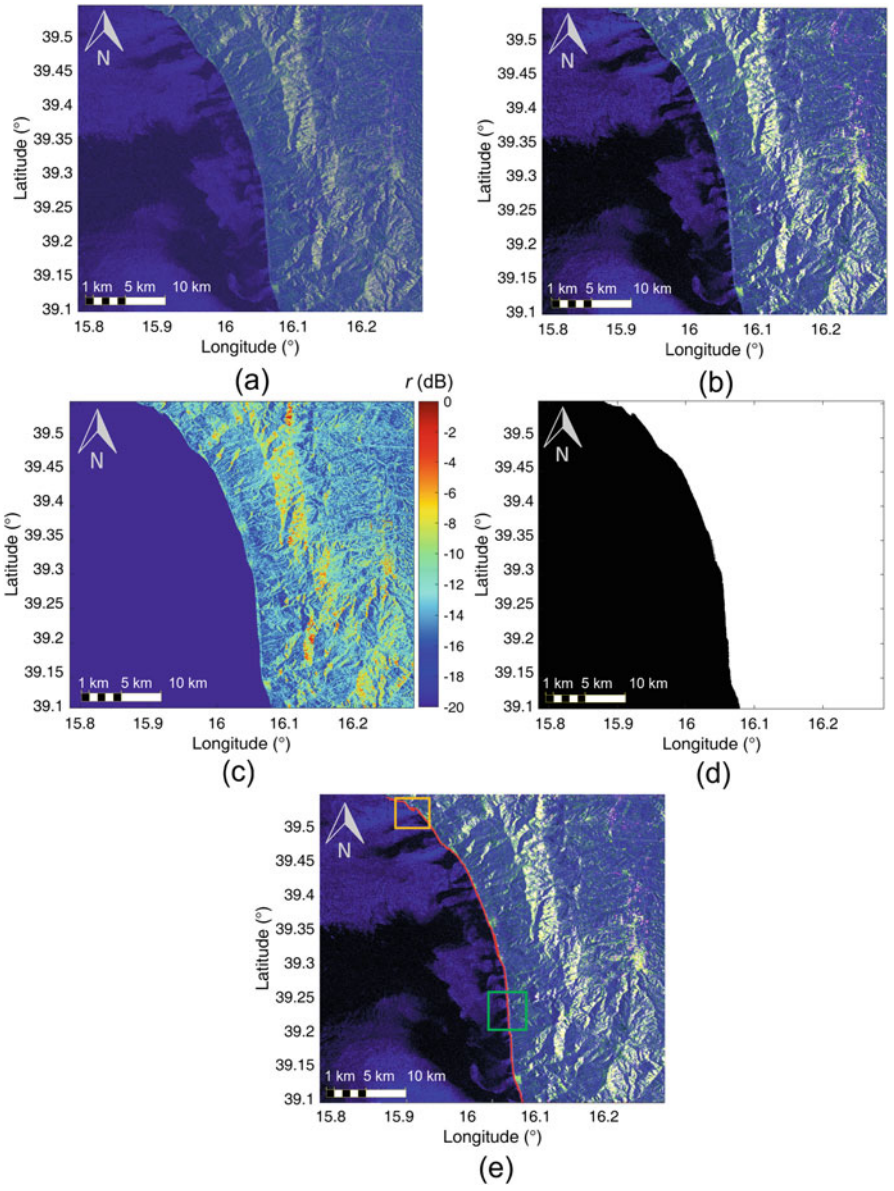

Fig. 13 Excerpt of Sentinel-1 SAR imagery collected over the coast of Calabria, Italy, on 11 July 2016. (**a**) RGB color composite (R: VV, G: VH, B: VV/VH power ratio) SAR imagery; (**b**) boxcar filtered RGB image using a window size 9 × 9; (**c**) r image in false color; (**d**) refined binary image obtained after the CFAR and the morphological filtering; (**e**) coastline extracted (in red) superimposed on RGB SAR image

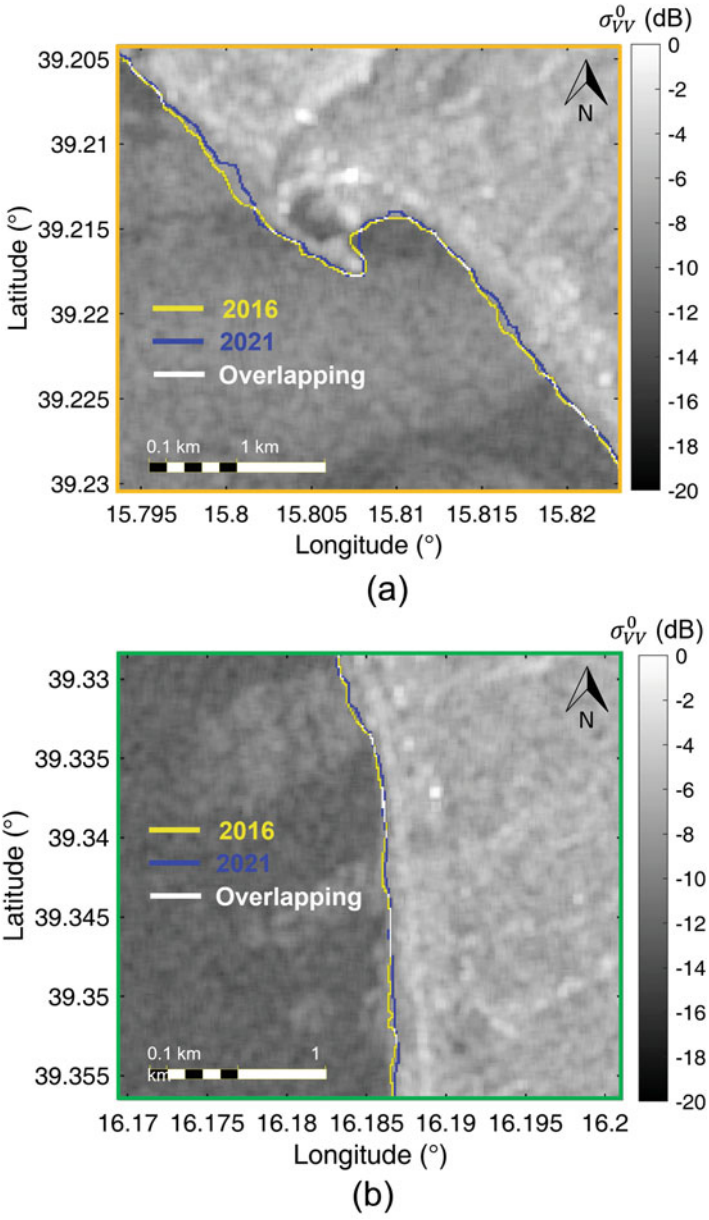

Fig. 14 Coastline extracted related to the SAR scene of: (**a**) Cetraro Marina (see yellow box of Fig. 13e); and (**b**) Marina di Belmonte (see green box of Fig. 13e). The coastlines, superimposed on the corresponding VV-polarized NRCS SAR image, are coded as yellow, blue, and white lines for 2016, 2021, and 2016–2021 overlapping, respectively

The second area, enclosed in the green box of Fig. 13e, refers to the coast of Marina di Belmonte, which is less affected by coastal erosion according to [28]. By visually inspecting Fig. 14b, it can be noted that the 2016 and 2021 coastlines are very close to each other, indicating that no significant changes occurred. A net erosion of 4.6×10^4 m^2 is estimated, i.e., about 40% less than the first test area.

4 Conclusions

In this chapter, the added value provided by polSAR satellite measurements in the framework of the monitoring of oceans and coastal areas is presented.

Section 1 deals with basic and advanced concepts of radar polarimetry that lie at the basis of the exploitation of polSAR data. Introduction to modeling of polarimetric sea surface scattering is also theoretically provided along with a meaningful experimental showcase.

Section 2 offers an overview of polarimetric approaches to observe sea oil spills from polSAR imagery. Benefits and drawbacks are critically pointed out. A though experimental showcase is also presented, which is based on the classification of ocean slicks using DL methods.

Section 3 provides the most up-to-date information on the use of polSAR measurements to extract coastal profiles and to monitor their changes over time. An experimental showcase is also discussed to highlight the potential of polSAR imagery to observe coastal areas affected by significant erosion processes.

The key message this chapter would convey to the reader is that a large set of polSAR measurements is nowadays available that can be successfully exploited to produce reliable and effective added-valued products and to develop advanced geophysical parameter estimation algorithms when proper electromagnetic models are considered.

Acknowledgments This chapter was written with the support of the ESA-NRCSS project Dragon 5 Monitoring harsh coastal environments and ocean surveillance using radar remote sensing sensors (ID 57979), the National Key R & D Program of China (2021YFA0715101), the Strategic Priority Research Program of Chinese Academy of Sciences (XDB 41020104), and Scientific Research Project of Beijing Educational Committee (KM202110005024).

The authors would thank the Alaska Satellite Facility Distributed Active Archive Center supported by the National Aeronautics and Space Administration for providing the Alos-PALSAR data. They would also thank ESA to provide free of charge the Sentinel-1 SAR data through the Copernicus Scientific Hub.

References

1. Ainsworth TL, Kelly JP, Lee JS (2009) Classification comparisons between dual-pol, compact polarimetric and quad-pol SAR imagery. ISPRS Journal of Photogrammetry & Remote Sensing 64(5):464–471

2. Bachofer F, Quénéhervé G, Zwiener T, Maerker M, Hochschild V (2016) Comparative analysis of edge detection techniques for SAR images. European Journal of Remote Sensing 49(1):205–224
3. Baghdadi N, Pedreros R, Lenotre N, Dewez T, Paganini M (2007) Impact of polarization and incidence of the ASAR sensor on coastline mapping: example of Gabon. International Journal of Remote Sensing 28(17):3841 – 3849
4. Bamler R (2000) Principles of synthetic aperture radar. Surveys in Geophysics
5. Bird E (2011) Coastal Geomorphology: An Introduction. Wiley
6. Brown CE, Fingas MF, Hawkins R (2003) Synthetic aperture radar sensors: Viable for marine oil spill response?
7. Buono A, Nunziata F, Mascolo L, Migliaccio M (2014) A multipolarization analysis of coastline extraction using X-band COSMO-SkyMed SAR data. IEEE Journal of Selected Topics on Applied Earth Observation and Remote Sensing 7(7):2811–2820
8. Buono A, Nunziata F, Migliaccio M (2016) Analysis of full and compact polarimetric SAR features over the sea surface. IEEE Geoscience and Remote Sensing Letters 13(10):1527–1531
9. Buono A, Nunziata F, Migliaccio M, Li X (2016) Polarimetric analysis of compact-polarimetry SAR architectures for sea oil slick observation. IEEE Transactions on Geoscience & Remote Sensing 54(10):5862–5874
10. Buono A, Nunziata F, de Macedo CR, Velotto D, Migliaccio M (2018) A sensitivity analysis of the standard deviation of the copolarized phase difference for sea oil slick observation. IEEE Transactions on Geoscience and Remote Sensing 57(4):2022–2030
11. Buono A, De Macedo CR, Nunziata F, Velotto D, Migliaccio M (2019) Analysis on the effects of SAR imaging parameters and environmental conditions on the standard deviation of the co-polarized phase difference measured over sea surface. Remote Sensing 11(1)
12. Buono A, Li Y, Paes RL (2021) Remote sensing of the oceans: Blue economy and marine pollution. Remote Sensing 13(8)
13. Carlo, Marangoni (1871) Sul principio della viscosita' superficiale dei liquidi stabilito dal sig. J. Plateau. Il Nuovo Cimento Series 2
14. Chen, Jie, Quegan, Shaun (2011) Calibration of spaceborne CTLR compact polarimetric low-frequency SAR using mixed radar calibrators. IEEE Transactions on Geoscience & Remote Sensing 49(7):2712–2723
15. Chen G, Li Y, Sun G, Zhang Y (2017) Application of deep networks to oil spill detection using polarimetric synthetic aperture radar images. Applied Sciences 7(10):968
16. Cloude S (2009) Polarisation: applications in remote sensing. OUP Oxford
17. Cloude SR, Goodenough DG, Chen H (2012) Compact decomposition theory. IEEE Geoscience and Remote Sensing Letters 9(1):28–32
18. Collins, M, J, Denbina, M, Atteia, G (2013) On the reconstruction of quad-pol SAR data from compact polarimetry data for ocean target detection. IEEE Transactions on Geoscience & Remote Sensing 51(1):591–600
19. Corcione V, Buono A, Nunziata F, Migliaccio M (2021) A sensitivity analysis on the spectral signatures of low-backscattering sea areas in Sentinel-1 SAR images. Remote Sensing 13(6)
20. Di Luccio D, Benassai G, Di Paola G, Mucerino L, Buono A, Rosskopf CM, Nunziata F, Migliaccio M, Urciuoli A, Montella R (2019) Shoreline rotation analysis of embayed beaches by means of in situ and remote surveys. Sustainability 11(3)
21. Di Martino G, Iodice A, Natale A, Riccio D (2016) Polarimetric two-scale two-component model for the retrieval of soil moisture under moderate vegetation via L-band SAR data. IEEE Transactions on Geoscience and Remote Sensing 54(4):2470–2491
22. Di Martino G, Iodice A, Monti-Guarnieri A (2020) Acquisition modes. In: Di Martino G, Iodice A (eds) Maritime Surveillance with Synthetic Aperture Radar, SciTech Publishing
23. Ding X, Nunziata F, Li X, Migliaccio M (2015) Performance analysis and validation of waterline extraction approaches using single- and dual-polarimetric SAR data. IEEE Journal of Selected Topics on Applied Earth Observation and Remote Sensing 8(3):1019 – 1027
24. Elfouhaily TM, Guérin CA (2004) A critical survey of approximate scattering wave theories from random rough surfaces. Waves in random media 14(4):R1

25. Espeseth MM, Skrunes S, Jones CE, Brekke C, Holt B, Doulgeris AP (2017) Analysis of evolving oil spills in full-polarimetric and hybrid-polarity SAR. IEEE Transactions on Geoscience and Remote Sensing 55(7):4190–4210
26. Espeseth MM, Brekke C, Jones CE, Holt B, Freeman A (2020) The impact of system noise in polarimetric SAR imagery on oil spill observations. IEEE Transactions on Geoscience and Remote Sensing 58(6):4194–4214
27. Espeseth MM, Jones CE, Holt B, Brekke C, Skrunes S (2020) Oil spill response-oriented information products derived from a rapid-repeat time-series of SAR images. IEEE Journal of Selected Topics in Applied Earth Observations and Remote Sensing PP(99):1–1
28. European Commission (2022) European Atlas of the Seas. URL https://ec.europa.eu/maritimeaffairs/atlas/maritime_atlas/
29. Ferrentino E, Nunziata F, Migliaccio M (2017) Full-polarimetric SAR measurements for coastline extraction and coastal area classification. International Journal of Remote Sensing 38(23):7405–7421
30. Ferrentino E, Nunziata F, Buono A, Urciuoli A, Migliaccio M (2020) Multipolarization time series of Sentinel-1 SAR imagery to analyze variations of reservoirs water body. IEEE Journal of Selected Topics in Applied Earth Observations and Remote Sensing 13:840 – 846
31. Ferrentino E, Buono A, Nunziata F, Marino A, Migliaccio M (2021) On the use of multipolarization satellite SAR data for coastline extraction in harsh coastal environments: The case of Solway Firth. IEEE Journal of Selected Topics in Applied Earth Observations and Remote Sensing 14:249–257
32. Franceschetti G, Riccio D, et al. (2002) Fractal models for scattering from natural surfaces. In: Scattering, Elsevier, pp 467–485
33. Gil JJ (2000) Characteristic properties of Mueller matrices. Journal of the Optical Society of America 17(2):328–334
34. Guissard A (1994) Mueller and Kennaugh matrices in radar polarimetry. IEEE Transactions on Geoscience and Remote Sensing 32(3):590–597
35. Guissard A, Sobieski P, Baufays C (1992) A unified approach to bistatic scattering for active and passive remote sensing of rough ocean surfaces. Trends of Geophysical Research 1:43–68
36. Hajnsek I, Pottier E, Cloude SR (2003) Inversion of surface parameters from polarimetric SAR. IEEE Transactions on Geoscience and Remote Sensing 41(4):727–744
37. Holt B (2004) SAR imaging of the ocean surface. Synthetic Aperture Radar Marine User's Manual (25–80)
38. Iodice A, Natale A, Riccio D (2011) Retrieval of soil surface parameters via a polarimetric two-scale model. IEEE Transactions on Geoscience and Remote Sensing 49(7):2531–2547
39. Ivonin D, Ivanov AY, Johansson AM, Brekke C (2021) Newly-formed sea ice distinction near the oil platform Prirazlomnaya in the Pechora Sea using polarimetric Radarsat-2 SAR observations. In: EUSAR 2021
40. Jie C, Quegan S (2010) Improved estimators of Faraday rotation in spaceborne polarimetric SAR data. IEEE Geoscience & Remote Sensing Letters 7(4):846–850
41. Kudryavtsev V, Hauser D, Caudal G, Chapron B (2003) A semiempirical model of the normalized radar cross-section of the sea surface 1. Background model. Journal of Geophysical Research: Oceans 108(C3):FET–2
42. Kudryavtsev V, Akimov D, Johannessen J, Chapron B (2005) On radar imaging of current features: 1. Model and comparison with observations. Journal of Geophysical Research: Oceans 110(C7)
43. Kudryavtsev VN, Chapron B, Myasoedov AG, Collard F, Johannessen JA (2012) On dual co-polarized SAR measurements of the ocean surface. IEEE Geoscience and Remote Sensing Letters 10(4):761–765
44. Kudryavtsev VN, Fan S, Zhang B, Mouche AA, Chapron B (2019) On quad-polarized SAR measurements of the ocean surface. IEEE Transactions on Geoscience and Remote Sensing 57(11):8362–8370
45. Kumar LJV, Kishore JK, Rao PK (2014) Decomposition methods for detection of oil spills based on RISAT-1 SAR

46. Laurentiis LD, Jones CE, Holt B, Schiavon G, Frate FD (2020) Deep learning for mineral and biogenic oil slick classification with airborne synthetic aperture radar data. IEEE Transactions on Geoscience and Remote Sensing 59(10):8455–8469
47. Lavalle M, Pottier E, Solimini D, Desnos YL (2009) Compact polarimetric SAR interferometry: PALSAR observations and associated reconstruction algorithms. ESA Special Publication
48. Lee JS, Pottier E (2017) Polarimetric radar imaging: from basics to applications. CRC press
49. Li BL, El-Shaarawi AH, Piegorsch WW (2002) Fractal dimensions. Encyclopedia of Environmetrics 2:821–825
50. Li H, Perrie W, He Y, Lehner S (2013) Target detection on the ocean with the relative phase of compact polarimetry SAR. IEEE Transactions on Geoscience and Remote Sensing 51(6 Part1):3299–3305
51. Li H, Perrie W, He Y, Wu J, Luo X (2015) Analysis of the polarimetric SAR scattering properties of oil-covered waters. IEEE Journal of Selected Topics in Applied Earth Observations & Remote Sensing 8(8):3751–3759
52. Li Y, Zhang Y, Chen J, Zhang H (2014) Improved compact polarimetric SAR quad-pol reconstruction algorithm for oil spill detection. IEEE Geoscience and Remote Sensing Letters 11(6):1139–1142
53. Melshelmer C, Alpers W, Gade M (1998) Investigation of multifrequency/multipolarization radar signatures of rain cells, derived from SIR-C/X-SAR data. In: International Geoscience & Remote Sensing Symposium
54. Meng T, Chen KS, Yang X, Nunziata F, Xie D, Buono A (2022) Simulation and analysis of bistatic radar scattering from oil-covered sea surface. IEEE Transactions on Geoscience and Remote Sensing 60:1–15
55. Meng T, Yang X, Chen KS, Nunziata F, Xie D, Buono A (2022) Radar backscattering over sea surface oil emulsions: Simulation and observation. IEEE Transactions on Geoscience and Remote Sensing 60:1–14
56. Migliaccio M, Nunziata F (2014) On the exploitation of polarimetric SAR data to map damping properties of the Deepwater Horizon oil spill. International Journal of Remote Sensing 35(10):3499–3519
57. Migliaccio M, Tranfaglia M (2005) A study on the use of SAR polarimetric data to observe oil spills. In: IEEE Oceans
58. Migliaccio M, Ferrara G, Gambardella A, Nunziata F (2006) A new stochastic model for oil spill observation by means of single-look SAR data. In: IEEE US/EU Baltic International Symposium, pp 24–29
59. Migliaccio M, Gambardella A, Tranfaglia M (2007) SAR polarimetry to observe oil spills. IEEE Transactions on Geoscience & Remote Sensing 45:506–511
60. Migliaccio M, Nunziata F, Gambardella A (2009) On the co-polarized phase difference for oil spill observation. International Journal of Remote Sensing 30(6):1587–1602
61. Migliaccio M, Nunziata F, Montuori A, Brown C (2011) Marine added-value products using Radarsat-2 fine quad-polarization. Canadian Journal of Remote Sensing 37(5):443–451
62. Migliaccio M, Nunziata F, Li X (2015) Sea oil slick observation using hybrid-polarity SAR architecture. IEEE Journal of Oceanic Engineering 40(2):426–440
63. Minchew B, Jones CE, Holt B (2012) Polarimetric analysis of backscatter from the Deepwater Horizon oil spill using L-band synthetic aperture radar. IEEE Transactions on Geoscience & Remote Sensing 50(10):3812–3830
64. Moon WM, Staples G, Kim D, Park S, Park K (2010) Radarsat-2 and coastal applications: Surface wind, waterline, and intertidal flat roughness. Proceedings of the IEEE 98(5):800 – 815
65. Nord ME, Ainsworth TL, Lee JS, Stacy NJS (2008) Comparison of compact polarimetric synthetic aperture radar modes. IEEE Transactions on Geoscience and Remote Sensing 47(1):174–188
66. Nunziata F, Sobieski P, Migliaccio M (2009) The two-scale BPM scattering model for sea biogenic slicks contrast. IEEE Transactions on Geoscience & Remote Sensing 47(7):1949–1956

67. Nunziata F, Migliaccio M, Gambardella A (2011) Pedestal height for sea oil slick observation. IET Radar Sonar & Navigation 5(2):103–110
68. Nunziata F, Migliaccio M, Li X, Ding X (2014) Coastline extraction using dual-polarimetric COSMO-SkyMed PingPong mode SAR data. IEEE Geoscience and Remote Sensing Letters 11(1):104 – 108
69. Nunziata F, Buono A, Migliaccio M, Benassai G (2016) Dual-polarimetric C- and X-band SAR data for coastline extraction. IEEE Journal of Selected Topics on Applied Earth Observation and Remote Sensing 9(11):4921 – 4928
70. Nunziata F, de Macedo CR, Buono A, Velotto D, Migliaccio M (2019) On the analysis of a time series of X–band TerraSAR–X SAR imagery over oil seepages. International Journal of Remote Sensing 40(9):3623–3646
71. Nunziata F, Li X, Marino A, Shao W, Portabella M, Yang X, Buono A (2021) Microwave satellite measurements for coastal area and extreme weather monitoring. Remote Sensing 13(16)
72. Plant W (1990) Bragg scattering of electromagnetic waves from the air/sea interface, surface waves and fluxes, vol. II. Remote Sensing, GL Geernaert and WL Plant, Eds, Kluwer Academic 10:978–94
73. Quigley C, Brekke C, Eltoft T (2020) Comparison between dielectric inversion results from synthetic aperture radar co-and quad-polarimetric data via a polarimetric two-scale model. IEEE Transactions on Geoscience and Remote Sensing 60:1–18
74. Quigley C, Brekke C, Eltoft T (2020) Retrieval of marine surface slick dielectric properties from Radarsat-2 data via a polarimetric two-scale model. IEEE Transactions on Geoscience and Remote Sensing 58(7):5162–5178
75. Raney RK (2007) Hybrid-polarity SAR architecture. In: IEEE International Conference on Geoscience & Remote Sensing Symposium
76. Scharf L, Demeure C (1991) Statistical Signal Processing: Detection, Estimation, and Time Series Analysis. Addison-Wesley series in electrical and computer engineering, Addison-Wesley Publishing Company
77. Shirvany R, Chabert M, Tourneret JY (2012) Ship and oil-spill detection using the degree of polarization in linear and hybrid/compact dual-pol SAR. IEEE Journal of Selected Topics in Applied Earth Observations and Remote Sensing 5(3):885–892
78. Skrunes S, Brekke C, Eltoft T (2014) Characterization of marine surface slicks by Radarsat-2 multipolarization features. IEEE Transactions on Geoscience & Remote Sensing 52(9):5302–5319
79. Skrunes S, Brekke C, Eltoft T, Kudryavtsev V (2014) Comparing near-coincident C- and X-band SAR acquisitions of marine oil spills. IEEE Transactions on Geoscience & Remote Sensing 53(4):1958–1975
80. Song D, Zhen Z, Wang B, Li X, Gao L, Wang N, Xie T, Zhang T (2020) A novel marine oil spillage identification scheme based on convolution neural network feature extraction from fully polarimetric SAR imagery. IEEE Access 8:59801–59820
81. Souyris JC, Stacy N, Ainsworth T, Lee JS, Dubois-Fernandez P (2014) SAR compact polarimetry (CP) for Earth observation and planetology: Concept and challenges
82. Stiassnie M, Agnon Y, Shemer L (1991) Fractal dimensions of random water surfaces. Physica D: Nonlinear Phenomena 47(3):341–352
83. Trabelsi C, Bilaniuk O, Zhang Y, Serdyuk D, Subramanian S, Santos JF, Mehri S, Rostamzadeh N, Bengio Y, Pal CJ (2017) Deep complex networks
84. Ulaby FT, Long DG, Blackwell WJ, Elachi C, Fung AK, Ruf C, Sarabandi K, Zebker HA, Van Zyl J (2014) Microwave radar and radiometric remote sensing, vol 4. University of Michigan Press Ann Arbor, MI, USA
85. Wang W, Fei L, Peng W, Wang J (2010) Oil spill detection from polarimetric SAR image. In: IEEE 10th International Conference on Signal Processing Proceedings
86. Yang J, Zhang X (2011) On the ship detection performance with compact polarimetry. IEEE National Radar Conference - Proceedings

87. Yeremy M, Beaudoin A, Beaudoin J, Walter G (2001) Global shoreline mapping from an airborne polarimetric SAR: Assessment for Radarsat-2 polarimetric modes p 66
88. Yin J, Yang J, Zhou ZS, Song J (2015) The extended Bragg scattering model-based method for ship and oil-spill observation using compact polarimetric SAR. IEEE Journal of Selected Topics in Applied Earth Observations & Remote Sensing 8(8):3760–3772
89. Yu L, Zhang Y, Jie C, Migliaccio M, Buono A (2016) Model-based sea surface scattering analysis for the DWH oil spill accident case. In: In Proceedings of IEEE International Geoscience and Remote Sensing Symposium
90. Yuanzhi Z, Yu L, Liang X, Jinyeu T (2017) Comparison of oil spill classifications using fully and compact polarimetric SAR images. Applied Sciences 7(2):193
91. Zhang, Yuanzhi, Li, Yu, Lin, Hui, Chen, Jie (2015) Comparisons of circular transmit and linear receive compact polarimetric SAR features for oil slicks discrimination. Journal of Sensors
92. Zhang B, Perrie W (2012) Cross-polarized synthetic aperture radar: A new potential measurement technique for hurricanes. Bulletin of the American Meteorological Society 93(4):531 – 541
93. Zhang B, Perrie W, Li X, Pichel WG (2011) Mapping sea surface oil slicks using Radarsat-2 quad-polarization SAR image. Geophysical Research Letters 38(10)